ELSEVIER

Comput. Methods Appl. Mech. Engrg. 190 (2000) 1551–1577

Computer methods in applied mechanics and engineering

www.elsevier.com/locate/cma

Computation of far-field solutions based on exact nonreflecting boundary conditions for the time-dependent wave equation

Lonny L. Thompson *, Runnong Huan

Department of Mechanical Engineering, Clemson University, Fluor Daniel Building, Clemson, SC 29634-0921, USA

Received 1 February 1999; received in revised form 12 March 1999

Abstract

In this work we show how to combine in the exact nonreflecting boundary conditions (NRBC) first derived by Grote and Keller, the calculation of the exterior (far-field) solution for time-dependent radiation and scattering in an unbounded domain. At each discrete time step, radial modes computed on a spherical artificial boundary which drive the exact NRBC for the near-field solution, are imposed as Cauchy data for the radial wave equation in the far-field. Similar to the far-field computation scheme used by Wright, the radial modes in the exterior region are computed using an explicit finite difference solver. However, instead of using an 'infinite grid', we truncate the exterior radial grid at the far-field point of interest, and for each harmonic, impose the same exact NRBC used for the near-field truncation boundary, here expressed in modal form. Using this approach, two different methods for extrapolating the near-field solution to the far-field are possible. In the first, the near-field solution is computed using the exact NRBC, then, based on the solution for the radial modes evaluated on the artificial boundary, the exterior solution may be computed as a *post-process*. In the second, we show how to compute the far-field solution *concurrently* with the near-field solution and the NRBC. Numerical studies demonstrate that the method is highly accurate and efficient for direct time-domain computations of far-field solutions.

1. Introduction

Interest in direct time-domain solutions of the scalar wave equation on unbounded domains follows from the need to accurately simulate radiation and scattering from pulse-driven structures of arbitrary shape. Direct time-domain solution allows for the efficient prediction of short-duration phenomena involving a wide range of frequencies. In addition to accurate solutions on the surface of the scatterer and in the near-field region surrounding the structure, results at some distance away from the radiator/scatterer are often of interest, such as far-field beam patterns and focal points.

In theory, the exact time-dependent solution may be determined from the retarded potential formulation of the well-known Kirchoff integral representation [1–3] applied on the surface of the scatterer. Since the Kirchoff formula makes no approximations beyond the homogeneity of the unbounded medium, the solution is valid whether the field point of interest is in the near-field or far-field. However, because the surface integrals must be discretized in both the temporal and spatial domains simultaneously, there is no efficient way of implementing Kirchoff's formula numerically for transient wave propagation. Due to convolution, the time history of all the surface points must be stored, resulting in large memory requirements. As they are nonlocal in both space and time, their numerical implementation can be computationally expensive. In fact, the order of the number of operations required by direct numerical

* Corresponding author. Tel.: +1-864-656-5631; fax: +1-864-656-4435.
E-mail address: lonny.thompson@ces.clemson.edu (L.L. Thompson).

0045-7825/00/$ - see front matter
PII: S0045-7825(00)00178-X

implementations of Kirchoff's formula is greater than that required by a simple explicit difference scheme for the wave equation in the exterior domain. In addition, numerical instabilities may result [4]. A stabilized version has recently been developed in [5], although the problem of the storage of time histories remains.

Finite element/difference/volume numerical methods are limited by the number of grid points required to accurately represent short wavelength components in a transient pulse. Generally, there must be at least 8–12 grid points per wavelength at the smallest wavelength of interest in the simulation to obtain accurate solutions. A direct approach to accurately compute far-field solutions is to exploit the finite wave speed c, in the medium, and extend the computational domain using an infinite grid so that the boundary cannot influence the solution in the region of interest for times less than the final time T. Far-field solutions obtained by these domain based computational methods would require field calculations in the region between the source and the distant points of interest. This would require a large mesh/grid of width of order $O(cT)$ with corresponding increase in computer expense and memory. Even with the use of explicit time-integrators, direct field calculations for points distant from a radiating structure or scatterer are generally impractical for moderate to large times.

To treat unbounded domains efficiently using a finite difference method or finite element method, the exterior field is truncated at an artificial boundary surrounding the source of scattering. The impedance of the exterior field is usually represented on this boundary by either approximate boundary conditions, infinite elements, or absorbing sponge layers, see [6,7] for extensive bibliographies. If accurate boundary treatments are used, the finite computational region (near-field) can be reduced so that the artificial boundary is relatively close to the radiator/scatterer, and fewer elements/grids than otherwise would be possible may be used, resulting in considerable savings in both CPU time and memory. The use of a finite element discretization for the near-field allows for a natural coupling to an elastic scatterer in applications of structural acoustics.

Efficient evaluation of accurate radiation boundary conditions for the time-dependent wave equation on unbounded spatial domains has long been an obstacle for the development of reliable solvers for time domain simulations. Ideally, the artificial boundary would be placed as close as possible to the scatterer, and the radiation boundary treatment would be capable of arbitrary accuracy at a cost and memory not exceeding that of the interior solver. If the form of the boundary treatment is over-simplified, spurious reflected waves can be generated at the artificial boundary, which can substantially degrade the accuracy of the numerical solution. For example, a standard approach is to apply local (differential) radiation boundary operators which annihilate leading terms in the radial expansion for outgoing wave solutions [8]. As the order of these local radiation boundary conditions increases they become increasingly difficult to implement in standard numerical methods due to the occurrence of high-order derivatives on the artificial boundary. Although most approximate boundary conditions perform well at nearly normal incidence to the artificial boundary, their accuracy deteriorates rapidly as grazing incidence is approached, especially as the artificial boundary is moved near the scatterer and for low frequencies [9–11]. In general, scattered and radiated waves arrive at the artificial boundary from several angles and frequencies, resulting in spurious reflections which tend to produce errors, which accumulate with time and prevent accurate medium to long time simulations. For accurate solutions, the use of approximate radiation boundary conditions requires that the truncation boundary be placed far away from the structure resulting in a large computational domain for the near-field solution with corresponding increase in computer memory and execution time. To verify the accuracy of the approximate boundary conditions, a series of computations must be performed, where the truncation boundary is progressively moved outward with more elements being added for each computation.

In recent years, a number of new boundary treatments have been developed, which have dramatically improved the accuracy and efficiency of time domain simulations. These new developments include fast spherical harmonic evaluation of exact, local in time boundary conditions on spherical boundaries [12–16], recursive methods of implementing high-order sequences of space and time localized radiation boundary conditions [17], rational approximations to the Dirichlet-to-Neumann (DtN) kernal [18], and absorbing sponge layers with reflectionless interfaces [19,20].

The first serious attempt to develop exact nonreflecting boundary conditions for the time-dependent wave equation is the treatment of Ting and Miksis [21,22], which makes use on the Kirchoff integral

formula on an artificial boundary Γ. This method uses a convolution integral requiring the storage of the solution at a surface inside the artificial boundary for the time needed for waves to propagate across the finite computational domain. While, this approach improves both cost and storage compared to direct implementation of the retarded potential form of the Kirchoff integral, it does not appear to be competitive on cost compared to equally accurate treatments discussed below.

In the frequency domain, it is well known that an exact nonreflecting boundary condition applied to a spherical boundary is available through Fourier or Laplace transform methods and the so-called DtN map [23,24]. The DtN map is a nonlocal (integral) operator obtained from the trace of the normal derivative of the solution on the truncation boundary. For efficient computation, it is most convenient to express the DtN map in terms of its eigenvalues and eigenfunctions on a separable boundary. For the special case of a sphere, the DtN representation simplifies as the eigenfunctions are spherical harmonics, which are independent of frequency, and the eigenvalues involve spherical Hankel functions, which may be represented in terms of simple rational functions. The rationality of the eigenvalues (DtN kernal) implies that the temporal convolution of the time-dependent counterpart can be localized, making computation efficient.

The time localization of the exact DtN boundary condition was first recognized and used in [12,13,25–28]. In [26], the time-convolution integral is approximated using special recurrence formulae. In [27,28], the convolution is replaced with high-order time-derivatives, which may be implemented in discontinuous Galerkin space-time finite element methods. In Grote and Keller [12], a local in time representation is obtained by solution of an auxiliary Cauchy problem for linear first-order systems of ordinary differential equations on the boundary for each spherical harmonic. In [14], the Grote and Keller form of the exact nonreflecting boundary condition (NRBC) is rederived based on the direct application of a result given in Lamb [29], with improved stability. The NRBC involves first-order derivatives only and does not require saving past values of the solution. The implementation of this local-in-time representation of the DtN map using finite difference methods is discussed in [13]. In [14] we showed how to implement the NRBC in a standard semidiscrete finite element formulation with several alternative implicit and explicit time-integrators. In [15], a modified version of the exact NRBC first derived in [13], is reformulated for implementation in the finite element method. The modified version may be viewed as an extension of the second-order local boundary operator derived by Bayliss and Turkel [8], and gives improved accuracy when only a few harmonics are included in the spherical expansion/transformation. When implemented in the finite element method, the NRBC's require inner products of spherical harmonics and standard C^0 continuous basis functions with compact support, appearing in the force vector. As a result, the NRBC may be computed using standard element assembly procedures, and does not modify the banded/sparse structure of the finite element matrix equations.

For a spherical boundary, the DtN may also be represented as a sequence of first-order differential equations in time with second-order local tangential derivatives of auxiliary functions on the boundary, [17]. Hagstrom and Hariharan indicated that these conditions can be effectively implemented in a finite difference scheme using only local tangential operators, but at the cost of introducing a large number of auxiliary functions at the artificial boundary. Direct finite element implementation of this sequence in a standard Galerkin variational equation would result in a nonsymmetric system of equations. In [16] we showed how the Hagstrom–Hariharan sequence may be derived based on the local boundary operators of Bayliss and Turkel [8]. For efficient implementation, the sequence of local boundary operators are written in terms of spherical harmonics and the recursive sequence is then reformulated as a Cauchy problem involving systems of first-order ordinary differential equations on the artificial boundary, similar to that used in [12,14]. With this reformulation, the resulting time local boundary conditions are implemented concurrently with standard semi-discrete finite element methods for the near-field solution without changing the banded/sparse structure of the finite element equations. With the number of equations in the Cauchy problem equal to the mode number, the reformulation is exact and can be shown to be equivalent to the NRBC derived in [12,14]. If fewer equations are used, then the boundary conditions form uniform approximations to the exact condition, allowing for reductions in memory and computational work, yet maintaining sufficient accuracy [16]. Furthermore, using this approach, accurate radiation boundary conditions may be efficiently implemented for the 2D unbounded problem on a circle [30].

For the scalar wave equation in an unbounded domain, several methods are available for extrapolating near-field solutions to the far-field. One approach is to save solutions on surfaces in the bounded computational domain (near-field) for later use as time-dependent boundary conditions in far-field computations. Direct application of Kirchoff's formula is often used to extrapolate the solution on a near-field sampling surface to the far-field [31,32]. However, this approach suffers from the problem of convolution of both the solution and normal derivative time-histories. While widely used in practice, the cost and memory requirements are high.

Another two-stage approach is given in [33], where the solution on a spherical surface close to the structure, which is independent of the truncation boundary, is saved for post-processing. Far-field solutions are computed using the previously saved solutions as time-dependent boundary conditions, and then by solving the external problem using a spherical harmonic expansion in the angular direction and the wave equation for the radial harmonics. The radial wave equation is discretized using an explicit finite difference scheme and an infinite grid in the radial coordinate extending beyond the far-field point of interest such that reflected waves from the boundary do not influence the solution, for times less than the final time of interest. In this approach, a large radial grid of length of order $O(cT)$ is required with corresponding increase in computational work. For moderate to long time intervals $I = [0, T]$, the amount of disk storage and data transfer required for this two-stage process may become excessive.

In this work, we develop a similar approach to the scheme used by Wright [33] and exploit a separable coordinate system to efficiently compute far-field solutions. Here, we take advantage of the exact NRBC derived in [12,14] written in terms of harmonics defined on the spherical artificial boundary to drive the solution to the exterior problem. We show how to combine in the Grote–Keller scheme the calculation of the exterior (far-field) solution. At each discrete time step, the radial modes computed using a spherical harmonic transform on the artificial boundary, and used for the near-field NRBC, are imposed as Cauchy data for the radial wave equation in the far-field. Following the discretization used in Wright [33], the radial modes in the exterior region are computed using an explicit finite difference solver and the method of characteristics. However, instead of using an infinite grid, we truncate the exterior radial grid at the far-field point of interest, and for each harmonic, impose the same exact NRBC used for the near-field truncation boundary, here expressed in modal form. If the point of interest is sufficiently far from the source of scattering, then the asymptotic form of the NRBC for large radius may be used a priori to save computational work. The solution at any point in the far-field is then computed from an inverse spherical harmonic transform of the far-field radial modes.

Using this approach, two different methods for extrapolating the near-field solution to the far-field are possible. In the first, the near-field solution is computed using the exact NRBC, then, based on the the solution for the radial modes evaluated on the artificial boundary, the exterior solution may be computed as a *post-process*. Since the total number of harmonics included in the series expansion for the NRBC is generally less than the number of grid points on the artificial boundary, and the spherical harmonic transform is computed only once, the amount of computation and disk storage is reduced compared to saving the entire solution on the artificial boundary surface. In the second method, we show how to compute the far-field solution *concurrently* with the near-field solution using the exact NRBC defined in [12,14]. In this approach, the radial modes on the artificial boundary are only computed as needed, so that past time-histories do not have to be saved.

In the following, we define the initial boundary value problem (IBVP) for both the near-field solution in the bounded domain defined by the introduction of an exact nonreflecting boundary condition on a spherical artificial boundary, and the far-field solution in the remaining unbounded domain exterior to this boundary. We then describe the space-time discretization used for the near- and far-field approximate solutions. To allow for natural coupling to elastic scatterers we use finite element discretization for the near-field. For accurate and efficient far-field solutions we use an explicit finite difference discretization of the radial wave equation. We then give a complete algorithm for computing the far-field solution concurrently with the near-field solution using Newmark's time-integration method for the near-field semidiscrete equations and the NRBC defined on the artificial boundary. Finally, numerical studies are performed to assess the accuracy of the far-field computation, both for individual harmonics, and for radiation and scattering problems involving an infinite number of harmonics in the solution.

2. Initial-boundary value problem for the exterior problem

We consider time-dependent scattering/radiation in an infinite 3D region. The boundary of the scatterer is denoted $\mathscr{S}$ with surrounding external region $\mathscr{R}$. Within $\mathscr{R}$ we assume the solution $\phi(\boldsymbol{x},t)$ is governed by the scalar wave equation. The IBVP for the scalar wave equation in the unbounded domain $\mathscr{R}$ may be stated as

$$\left[\frac{1}{c^2}\frac{\partial^2}{\partial t^2}-\nabla^2\right]\phi(\boldsymbol{x},t)=f(\boldsymbol{x},t),\quad \boldsymbol{x}\in\mathscr{R},\ \ t\geqslant 0, \tag{1}$$

$$\phi(\boldsymbol{x},0)=\phi_0(\boldsymbol{x}),\quad \boldsymbol{x}\in\mathscr{R}, \tag{2}$$

$$\dot{\phi}(\boldsymbol{x},0)=\dot{\phi}_0(\boldsymbol{x}),\quad \boldsymbol{x}\in\mathscr{R}, \tag{3}$$

$$\alpha\frac{\partial\phi}{\partial n}+\beta\frac{\partial\phi}{\partial t}+\gamma\phi=g(\boldsymbol{x},t),\quad \boldsymbol{x}\in\mathscr{S},\ \ t\geqslant 0, \tag{4}$$

where $f,g,\phi_0,\dot{\phi}_0$ are the prescribed data. The wave speed c and α,β,γ are real, and we assume $c>0$, $\alpha,\beta\geqslant 0$.

In the far-field, ϕ satisfies the outgoing wave condition at infinity [34]

$$\lim_{r\to\infty} r\left(\frac{\partial}{\partial r}+\frac{1}{c}\frac{\partial}{\partial t}\right)\phi=0, \tag{5}$$

where $r=\|\boldsymbol{x}\|$ is the radial distance from the source.

2.1. Near-field solution

For the near-field solution, the unbounded region $\mathscr{R}$ is truncated by an artificial spherical boundary Γ, of radius R. We then denote by $\Omega\subset\mathscr{R}$ the finite subdomain bounded by Γ and $\mathscr{S}$, see Fig. 1. The source f and initial data ϕ_0 and $\dot{\phi}_0$ are assumed to be confined to the interior of the sphere, i.e.,

$$f(\boldsymbol{x},t)=0,\quad \phi_0(\boldsymbol{x})=0,\quad \dot{\phi}_0(\boldsymbol{x})=0 \tag{6}$$

for $r=\|\boldsymbol{x}\|\geqslant R$.

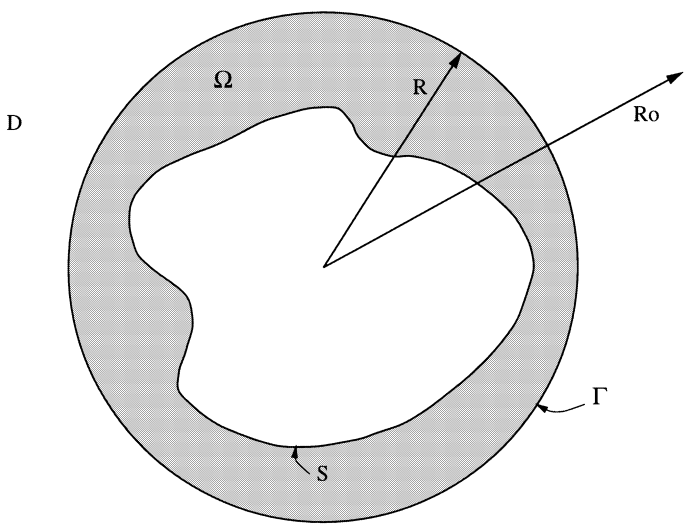

Fig. 1. Illustration of infinite region $\mathscr{R}$ surrounding a scatterer $\mathscr{S}$. The near-field bounded domain $\Omega\subset\mathscr{R}$ is surrounded by a spherical truncation boundary Γ. Exterior region denoted by $\mathscr{D}=\mathscr{R}-\Omega$, with far-field radius R_0.

The IBVP for the solution $\phi(\boldsymbol{x},t):\Omega\times[0,T]\mapsto\mathbb{R}$, in the bounded domain Ω may be stated as

$$\left[\frac{1}{c^2}\frac{\partial^2}{\partial t^2}-\nabla^2\right]\phi(\boldsymbol{x},t)=f(\boldsymbol{x},t),\quad \boldsymbol{x}\in\Omega,\ \ t\geqslant 0, \tag{7}$$

$$\phi(\boldsymbol{x},0)=\phi_0(\boldsymbol{x}),\quad \boldsymbol{x}\in\Omega, \tag{8}$$

$$\dot{\phi}(\boldsymbol{x},0)=\dot{\phi}_0(\boldsymbol{x}),\quad \boldsymbol{x}\in\Omega, \tag{9}$$

$$\alpha\frac{\partial\phi}{\partial n}+\beta\frac{\partial\phi}{\partial t}+\gamma\phi=g(\boldsymbol{x},t),\quad \boldsymbol{x}\in\mathscr{S},\ \ t\geqslant 0 \tag{10}$$

supplemented by the exact nonreflecting boundary condition (NRBC) on Γ, first derived by Grote and Keller [12], and modified with improved scaling in [14]

$$B_1[\phi(\boldsymbol{x},t)]=-\frac{1}{R}\sum_{n\geqslant 1}\sum_{|m|\leqslant n}\boldsymbol{c}_n\cdot\boldsymbol{z}_{nm}(t)Y_{nm}(\theta,\varphi)\quad\text{on }\Gamma,\ \ t\geqslant 0. \tag{11}$$

The local differential operator,

$$B_1[\phi]:=\left(\frac{\partial}{\partial r}+\frac{1}{c}\frac{\partial}{\partial t}+\frac{1}{r}\right)\phi \tag{12}$$

is the first-order condition of Bayliss and Turkel [8], which annihilates the leading radial term in outgoing solutions to the wave equation. The functions Y_{nm} in the expansion are orthogonal spherical harmonics normalized on the unit sphere

$$Y_{nm}(\theta,\varphi)=[(2n+1)(n-|m|)!/4\pi(n+|m|)!]^{1/2}\mathrm{e}^{\mathrm{i}m\varphi}P_n^{|m|}(\cos\theta) \tag{13}$$

for $0\leqslant\theta<\pi$ and $0\leqslant\varphi\leqslant 2\pi$. The coefficients involve the inner product of the constant vector $\boldsymbol{c}_n=\{c_n^j\}$,

$$c_n^j=(n(n+1)j)/2R,\quad j=1,\ldots,n \tag{14}$$

and the time-dependent vector $\boldsymbol{z}_{nm}(t)$, which satisfies the first-order system of ordinary differential equations,

$$\frac{\mathrm{d}}{\mathrm{d}t}\boldsymbol{z}_{nm}(t)=\boldsymbol{A}_n\boldsymbol{z}_{nm}(t)+c\phi_{nm}(R,t)\boldsymbol{e}_1 \tag{15}$$

with initial conditions $\boldsymbol{z}_{nm}(0)=0$, and driven by the radial modes,

$$\phi_{nm}(R,t)=\int_0^{2\pi}\int_0^{\pi}Y_{nm}^*(\theta,\varphi)\phi(R,\theta,\varphi,t)\sin\theta\,\mathrm{d}\theta\,\mathrm{d}\varphi. \tag{16}$$

Here, the star indicates complex conjugate. Alternatively, real spherical harmonics may be used, given by the real and imaginary parts of (13) with a modification to the normalization constant. In (15), the constant $n\times n$ coefficient matrix $\boldsymbol{A}_n=\{A_n^{ij}\}$, is defined as [14]

$$A_n^{ij}=\frac{c}{R}\begin{cases}\dfrac{-n(n+1)}{2} & \text{if } i=1,\\[2mm] \dfrac{(n+i)(n-i+1)}{2i} & \text{if } i=j+1\\[2mm] 0 & \text{otherwise}\end{cases} \tag{17}$$

and $\boldsymbol{e}_1=\{e_1^j\}$ is the constant unit vector,

$$\boldsymbol{e}_1=[1,0,\ldots,0]^{\mathrm{T}}. \tag{18}$$

The boundary condition (11) is termed *exact* since the truncated problem has a unique solution which, for all $t>0$, coincides with the restriction to Ω of the solution of the original problem posed on the unbounded

domain $\mathscr{R}$, [13]. In computation, the infinite sum over n in (11) is truncated at a finite value N. We denote the boundary condition (11) by NR1(N), where N defines the number of harmonics included in the truncated series. Use of (11) on a spherical boundary Γ will exactly represent all harmonics ϕ_{nm}, for $n \leqslant N$. For $n > N$, the truncated condition (11) approximates the harmonics with the local operator $B_1[\phi] = 0$ on Γ, with leading error of order, $B_1[\phi] = \mathcal{O}(\frac{1}{R^3})$. Accuracy of the approximated harmonics $n > N$, may be improved by increasing the radius of the truncation boundary R, but at the added expense of a larger computation region Ω, resulting in increased memory and CPU times.

To improve the approximation to the truncated harmonics $n > N$, without affecting the modes $n \leqslant N$, (11) may be replaced with a modified condition [15],

$$B_2[\phi(\boldsymbol{x},t)] = \frac{1}{R}\sum_{n\geqslant 2}\sum_{|m|\leqslant n}\tilde{\boldsymbol{c}}_n\cdot\boldsymbol{z}_{nm}(t)Y_{nm}(\theta,\varphi) \quad \text{on } \Gamma,\ \ t\geqslant 0, \tag{19}$$

where $\tilde{\boldsymbol{c}}_n = \{\tilde{c}_n^j\}$

$$\tilde{c}_n^j = n(n+1)j(j-1)/2R^2, \quad j = 1,\ldots,n \tag{20}$$

and

$$B_2[\phi] := \frac{2}{c}\frac{\partial}{\partial t}B_1[\phi] + \frac{2}{R}B_1[\phi] - \frac{1}{R^2}\Delta_\Gamma[\phi] \tag{21}$$

is the local second-order operator of Bayliss and Turkel [8] with second-order radial derivatives eliminated in favor of tangential derivatives on the boundary Γ, through use of the wave equation in spherical coordinates. The tangential derivatives are given by the Laplace–Beltrami operator,

$$\Delta_\Gamma[\phi] =: \frac{1}{\sin\theta}\frac{\partial}{\partial\theta}\left(\sin\theta\frac{\partial\phi}{\partial\theta}\right) + \frac{1}{\sin^2\theta}\frac{\partial^2\phi}{\partial\varphi^2}. \tag{22}$$

The vector functions $\boldsymbol{z}_{nm}(t)$ appearing in (19) satisfy the same first-order system of ordinary differential Eq. (15), driven by (16). In practice, the sum over n in (19) is truncated at a finite value N. For $n > N$, the truncated condition (19) reduces to $B_2[\phi] = 0$ on Γ. This condition approximates the harmonics $n > N$, with leading error of order, $B_2[\phi] = \mathcal{O}(1/R^5)$. Therefore, when truncated at a finite value N, the NRBC (19) approximates the modes $n > N$ with greater accuracy than (11).

In [15], we show how the modified boundary condition (19) can be implemented in a symmetric finite element variational formulation by introducing additional auxiliary functions $q_{nm}(t)$ and $\psi(\theta,\varphi,t)$, such that

$$B_1[\phi] - \frac{1}{2R}\Delta_\Gamma[\psi] = \frac{1}{2}\sum_{n=2}^{\infty}\sum_{m=-n}^{n}q_{nm}(t)Y_{nm} \quad \text{on } \Gamma,\ \ t\geqslant 0, \tag{23}$$

$$\left(\frac{R}{c}\frac{\partial}{\partial t}+1\right)\Delta_\Gamma[\psi] = \Delta_\Gamma[\phi], \quad \psi(\theta,\varphi,0) = 0, \tag{24}$$

$$\left(\frac{R}{c}\frac{\mathrm{d}}{\mathrm{d}t}+1\right)q_{nm}(t) = \tilde{\boldsymbol{c}}_n\cdot\boldsymbol{z}_{nm}(t), \quad q_{nm}(0) = 0. \tag{25}$$

The three (23)–(25), define an equivalent form of the exact NRBC (19), suitable for implementation in a symmetric finite element formulation.

Alternatively, based on the recursive sequence of local boundary operators given in [17], we show in [16] that the exact nonreflecting boundary conditions (11) and (19) may be reformulated as

$$B_1[\phi(\boldsymbol{x},t)] = \sum_{n\geqslant 1}\sum_{|m|\leqslant n}v_{nm,1}(t)Y_{nm}(\theta,\varphi) \quad \text{on } \Gamma,\ \ t\geqslant 0 \tag{26}$$

and

$$B_2[\phi(\boldsymbol{x},t)] = 2\sum_{n\geqslant 2}\sum_{|m|\leqslant n} v_{nm,2}(t)Y_{nm}(\theta,\varphi) \quad \text{on } \Gamma,\ \ t\geqslant 0, \tag{27}$$

respectively, with time-dependent vector $\boldsymbol{v}_{nm}(t) = \{v_{nm,j}(t)\}$, $j = 1,\ldots,l$, such that

$$\frac{\mathrm{d}}{\mathrm{d}t}\boldsymbol{v}_{nm}(t) = \boldsymbol{C}_n\boldsymbol{v}_{nm}(t) - a_n\,\phi_{nm}(R,t)\boldsymbol{e}_1 \tag{28}$$

and banded, tridiagonal matrix $\boldsymbol{C}_n = [C_n]_{ij}$ defined by,

$$[C_n]_{ij} = \frac{c}{R}\begin{cases} -i & \text{if } i = j, \\ R & \text{if } i = j-1, \\ [i(i-1)-n(n+1)]/4R & \text{if } i = j+1, \\ 0 & \text{otherwise} \end{cases} \tag{29}$$

and $a_n = n(n+1)c/2R^2$.

With $l = n$, then $v_{nm,n+1} = 0$ and the boundary condition is exact. The auxiliary functions satisfy the property, $v_{nm,j+1} < v_{nm,j}$, and $v_{nm,j} = \mathrm{O}(R^{-2j-1})$, and thus may be implemented as an asymptotic boundary condition, with fewer equations, $l < n$, see [16]. In this form, the functions $\boldsymbol{v}_{nm}$ are interpreted as residuals of the local operators acting on a multi-pole expansion, and may be implemented with seperate variations on the radial and transverse modal orders of the radiation boundary condition.

2.2. Far-field solution

The far-field solution is the restriction of $\phi(\boldsymbol{x},t)$ for $r = \|\boldsymbol{x}\| \geqslant R$. With the source $f(\boldsymbol{x},t)$ and initial data confined to the bounded domain Ω, then in the exterior region $\mathscr{D} = \mathscr{R} - \Omega$, i.e., the unbounded domain outside Γ, the scalar field $\phi(\boldsymbol{x},t)$ satisfies the homogeneous form of the wave equation, driven by the near-field solution evaluated at $r = R$

$$\left[\frac{1}{c^2}\frac{\partial^2}{\partial t^2} - \nabla^2\right]\phi(\boldsymbol{x},t) = 0, \quad \boldsymbol{x}\in\mathscr{D},\ \ t\geqslant 0, \tag{30}$$

$$\phi(\boldsymbol{x},0) = 0, \quad \boldsymbol{x}\in\mathscr{D}, \tag{31}$$

$$\dot{\phi}(\boldsymbol{x},0) = 0, \quad \boldsymbol{x}\in\mathscr{D}, \tag{32}$$

$$\phi(\boldsymbol{x},t) = \phi(R,\theta,\varphi,t), \quad \boldsymbol{x}\in\Gamma,\ \ t\geqslant 0 \tag{33}$$

$$\lim_{r\to\infty} r\left(\frac{\partial}{\partial r} + \frac{1}{c}\frac{\partial}{\partial t}\right)\phi = 0. \tag{34}$$

In (33), $\phi(R,\theta,\varphi,t)$ is the trace of the solution for the interior problem on Γ.

In order to efficiently compute the far-field solution in $\mathscr{D}$, we transform the problem using spherical harmonics, and take advantage of the fact that every function on the surface of a sphere (specifically, every function whose square is integrable) can be expanded in a series of spherical harmonics

$$\phi(r,\theta,\varphi,t) = \sum_{n\geqslant 0}\sum_{|m|\leqslant n}\phi_{nm}(r,t)Y_{nm}(\theta,\varphi), \tag{35}$$

where

$$\Delta_\Gamma Y_{nm} = -n(n+1)Y_{nm} \tag{36}$$

and each mode $\phi_{nm}(r,t)$ satisfies the radial wave equation,

$$\frac{1}{c^2}\frac{\partial^2\phi_{nm}}{\partial t^2} = \frac{1}{r^2}\left[\frac{\partial}{\partial r}\left(r^2\frac{\partial}{\partial r}\right) - n(n+1)\right]\phi_{nm}, \quad r\geqslant R,\ \ t\geqslant 0, \tag{37}$$

$$\phi_{nm}(r,0)=0, \qquad \frac{\partial\phi_{nm}}{\partial t}(r,0)=0, \quad r\geqslant R. \tag{38}$$

On the truncation boundary Γ, at $r=R$, the near-field solution is expanded as,

$$\phi(R,\theta,\varphi,t)=\sum_{n\geqslant 0}\sum_{|m|\leqslant n}\phi_{nm}(R,t)Y_{nm}(\theta,\varphi) \tag{39}$$

and the radial modes are computed from the spherical harmonic transform,

$$\phi_{nm}(r,t)=(\phi,Y_{nm}):=\int_0^{2\pi}\int_0^{\pi}Y^*_{nm}(\theta,\varphi)\phi(r,\theta,\varphi,t)\sin\theta\,\mathrm{d}\theta\,\mathrm{d}\varphi \tag{40}$$

evaluated at $r=R$, i.e., $\phi_{nm}(R,t)=(\phi|_R,Y_{nm})$. The spherical harmonic transform defines an inner product involving integration with respect to θ and φ on a sphere of radius r.

In the far-field $\mathscr{D}$, at position $r=R_0$, with $R<R_0<\infty$, the radial functions $\phi_{nm}(R_0,t)$ satisfy the modal form of the exact boundary condition given in (11)

$$B_1[\phi_{nm}]=-\frac{1}{r}\boldsymbol{d}_n\cdot\boldsymbol{w}_{nm}(t), \quad r=R_0, \tag{41}$$

where B_1 is the local operator (12) and $\boldsymbol{w}_{nm}(t)=\{w^j_{nm}(t)\}$, $j=1,\ldots,n$ are vector functions of order n, which satisfy the first-order system of ordinary differential Eq. (15) with R, replaced with R_0, i.e.,

$$\begin{aligned}&\frac{\mathrm{d}}{\mathrm{d}t}\boldsymbol{w}_{nm}(t)=\boldsymbol{B}_n\boldsymbol{w}_{nm}(t)+c\phi_{nm}(R_0,t)\boldsymbol{e}_1,\\&\boldsymbol{w}_{nm}(0)=0\end{aligned} \tag{42}$$

Here $\boldsymbol{B}_n=\{B^{ij}_n\}$ is the constant $n\times n$ matrix,

$$B^{ij}_n=\frac{c}{R_0}\begin{cases}\dfrac{-n(n+1)}{2} & \text{if } i=1,\\[2mm] \dfrac{(n+i)(n-i+1)}{2i} & \text{if } i=j+1,\\[2mm] 0 & \text{otherwise.}\end{cases} \tag{43}$$

The constant n-component vector $\boldsymbol{d}_n=\{d^j_n\}$ is defined as,

$$d^j_n=n(n+1)j/2R_0, \quad j=1,\ldots,n. \tag{44}$$

Using (35) and (41), the extension of the near-field solution on Γ, to the far-field $\mathscr{D}$, reduces to solving the modes $u(r,t)=r\phi_{nm}(r,t)$, for $n\geqslant 0$, and $|m|\leqslant n$ in the region $R\leqslant r\leqslant R_0$. Each mode $n=0,\ldots,N$, satisfies the following modified radial wave equation with homogeneous initial data, and driven by the near-field solution evaluated at $r=R$

$$\left[\frac{1}{c^2}\frac{\partial^2}{\partial t^2}-\frac{\partial^2}{\partial r^2}+\frac{n(n+1)}{r^2}\right]u(r,t)=0, \quad R\leqslant r\leqslant R_0, \ \ t\geqslant 0, \tag{45}$$

$$u(r,0)=0, \quad R\leqslant r\leqslant R_0, \tag{46}$$

$$\dot{u}(r,0)=0, \quad R\leqslant r\leqslant R_0, \tag{47}$$

$$u(R,t)=R(\phi|_R,Y_{nm}), \quad t\geqslant 0, \tag{48}$$

$$\left(\frac{\partial}{\partial r}+\frac{1}{c}\frac{\partial}{\partial t}\right)u(r,t)=-\boldsymbol{d}_n\cdot\boldsymbol{w}_{nm}(t), \quad r=R_0, t\geqslant 0, \tag{49}$$

and $\boldsymbol{w}_{nm}$ satisfies (42). In practice, we restrict $0 \leqslant n \leqslant N$, and the solution at any point (r, θ, φ), for $R < r \leqslant R_0$, is computed from the spherical harmonic evaluation (35) truncated at the finite value N. We denote the application of the NRBC (49), for each mode n, as NR1. This boundary condition does not require saving past values of u, which would be required in a Kirchoff-type time convolution. Instead, the boundary condition involves the solution of the functions $\boldsymbol{w}_{nm}(t)$ in (42), which can be computed efficiently with standard time-integration. The memory needed to store these functions is approximately N^3 scalar values. The extra work in applying the boundary condition results from computing the inner products in the spherical harmonic transform (48) and the evaluation (35). In computation, we have found $N \leqslant 25$ is usually sufficient for accurate solutions. If a large number of harmonics N are needed, the work required could be reduced by an order of magnitude using recently developed fast spherical transform algorithms, e.g., [35,36], to compute the inner products. For mode $n = 0$, the exact nonreflecting boundary condition (49) simplifies to the local B_1 operator, which requires no storage and little extra work. Furthermore, for modes $n = 1, 2, \ldots$, the radiation condition (49) reduces to the local B_1 boundary operator in the asymptotic limit $R_0 \to \infty$. To see this, let $\mathscr{F}$ denote the Fourier transform with respect to frequency ω, defined as the dual of time t, and define $\mathscr{F}^{-1}$ as its inverse

$$\hat{\phi}_{nm}(r, \omega) = \mathscr{F}\phi_{nm}(r, t) := \frac{1}{\sqrt{2\pi}} \int_{-\infty}^{\infty} \phi_{nm}(r, t) \mathrm{e}^{\mathrm{i}\omega t} \, \mathrm{d}t. \tag{50}$$

In the frequency domain, time-harmonic solutions to the radial wave equation take the form,

$$\hat{\phi}_{nm}(r, \omega) = \frac{h_n(kr)}{h_n(kR_0)} \hat{\phi}_{nm}(R_0, \omega), \tag{51}$$

where $k = \omega/c$ is the wavenumber and $h_n(kr)$ are spherical Hankel functions of the first kind [37]. Computing the trace of the normal derivative of the solution at $r = R_0$, defines the Dirichlet-to-Neumann map for each mode,

$$\frac{\partial \hat{\phi}_{nm}}{\partial r}(R_0, \omega) = \frac{kh_n'(kR_0)}{h_n(kR_0)} \hat{\phi}_{nm}(R_0, \omega). \tag{52}$$

In the asymptotic limit $kR_0 \gg n^2 + 1$, the DtN map reduces to,

$$\frac{kh_n'(kR_0)}{h_n(kR_0)} \sim ik - \frac{1}{R_0} \tag{53}$$

Taking the inverse Fourier transform of the asymptotic expansion for the DtN map gives,

$$\frac{\partial \phi_{nm}}{\partial r}(R_0, t) = \mathscr{F}^{-1}\left(ik - \frac{1}{R_0}\right) \hat{\phi}_{nm}(R_0, \omega), \tag{54}$$

which defines the local B_1 operator,

$$B_1[\phi_{nm}(r, t)] := \left(\frac{\partial}{\partial r} + \frac{1}{c}\frac{\partial}{\partial t} + \frac{1}{r}\right)\phi_{nm}(r, t) = 0, \quad r = R_0. \tag{55}$$

Comparing with (49), in the asymptotic limit, $\boldsymbol{d}_n \cdot \boldsymbol{w}_{nm}(t) \sim 0$, and for a finite frequency range, the radiation boundary condition for each mode $u = r\phi_{nm}$ tends to the local B_1 condition,

$$\left(\frac{\partial}{\partial r} + \frac{1}{c}\frac{\partial}{\partial t}\right)u(r, t) = 0, \quad r \to \infty. \tag{56}$$

Thus if the far-field point is sufficiently distant from the source of radiation, such that $kR_0 \gg n^2 + 1$, the exact boundary condition for modes $n \ll \sqrt{kR_0 - 1}$, may be simplified a-priori to the local B_1 condition.

3. Numerical formulation

The near-field problem can be solved using any finite domain computation method, e.g., finite element or finite difference. Grote and Keller [13] discuss implementation of (11) and (19) using a finite difference method. In [14,15], we show how to implement (11) and (19), in a standard semidiscrete finite element formulation with several alternative implicit and explicit time-integrators. The use of a finite element discretization for the near-field allows for a natural coupling to an elastic scatterer in applications of structural acoustics.

For the far-field problem, discretization of the radial wave equation (37), or equivalently (45), may be performed either with the finite difference method or finite element method. For accurate and efficient solutions, it is sufficient to use an explicit finite difference method. Adaptive finite element discretization may be used together with a posteriori error estimation to track transient wave pulses along characteristics, but this is not pursued here.

3.1. Space-time discretization for the near-field

The finite element discretization for the near-field is obtained by approximating the variational equation associated with (7)–(9), (9)–(11). The variational equation within Ω is obtained by multiplying (7) with a weighting function and using the divergence theorem [14]. The domain is discretized into a finite number of subdomains (elements), associated with a finite number of nodes. Using a standard Galerkin finite element approximation $\phi(\boldsymbol{x},t) \approx \boldsymbol{N}(x)\boldsymbol{\phi}(t)$, where $\boldsymbol{N}(\boldsymbol{x})$ is a vector array of C° basis functions with compact support associated with each node, results in standard semidiscrete equations for the global solution vector $\boldsymbol{\phi}(t)$

$$\boldsymbol{M}\ddot{\boldsymbol{\phi}}(t) + \boldsymbol{C}\dot{\boldsymbol{\phi}}(t) + \boldsymbol{K}\boldsymbol{\phi}(t) = \boldsymbol{F}(t), \quad t > 0, \tag{57}$$

$$\boldsymbol{\phi}(0) = \boldsymbol{\phi}_0, \qquad \dot{\boldsymbol{\phi}}(0) = \dot{\boldsymbol{\phi}}_0. \tag{58}$$

In the above, $\boldsymbol{M}$, $\boldsymbol{C}$, and $\boldsymbol{K}$ are standard banded/sparse arrays associated with the discretization of the wave equation and the local B_1 operator; and $\boldsymbol{F}(t) = \boldsymbol{F}_S + \boldsymbol{F}_\Gamma$ is the discrete force vector composed of a standard load vector $\boldsymbol{F}_S$ and a part associated with the auxiliary functions appearing in the NRBC. For the NRBC defined in (11), the force vector is,

$$\boldsymbol{F}_\Gamma(t) = -\frac{1}{R}\sum_{n=1}^{N}\sum_{m=-n}^{n} \boldsymbol{c}_n \cdot \boldsymbol{z}_{nm}(t)\boldsymbol{f}_{nm}, \tag{59}$$

where,

$$\boldsymbol{f}_{nm} := \int_\Gamma \boldsymbol{N}^{\mathrm{T}} Y_{nm}(\theta,\varphi)\, \mathrm{d}\Gamma. \tag{60}$$

In (59), the functions $\boldsymbol{z}_{nm} = \{z^j_{nm}\}$ are solutions to the system of first-order Eq. (15), driven by,

$$\phi_{nm}(R,t) = \boldsymbol{f}^{*\mathrm{T}}_{nm} \cdot \boldsymbol{\phi}_\Gamma(t), \tag{61}$$

where $\boldsymbol{\phi}_\Gamma(t) = \{\phi_I(t)\}$, $I = 1,2,\ldots,N_\Gamma$, is a vector of nodal solutions on the artificial boundary Γ with N_Γ nodes. The nonreflecting boundary condition only requires inner products of spherical harmonics and finite element basis functions with compact support within the force vector $\boldsymbol{f}_{nm}$. As a result, the nonreflecting boundary condition is easy to implement using standard force vector assembly over each boundary element on Γ, and does not disturb the symmetric, and banded/sparse structure of the finite element matrix equations.

As discussed in [14], one time-integration approach is to apply the central difference method directly to (57). This method requires only that the forcing term $\boldsymbol{F}^k = \boldsymbol{F}(t_k)$ at time step $t_k = k\Delta t$, be available. Therefore, to update the solution $\boldsymbol{d}^{k+1} = \boldsymbol{\phi}(t_{k+1})$, only the evaluation of $\boldsymbol{z}^k_{nm} = \boldsymbol{z}_{nm}(t_k)$ is needed. In this case, $\boldsymbol{z}^{k+1}_{nm}$ may be computed using either the explicit second-order Adams–Bashforth method or the implicit second-order Adams–Moulton method (trapezoidal rule).

An alternative approach is to apply the Newmark family of algorithms (and variations such as HHT-α) in predictor/corrector form to the semidiscrete equations (57) [14]:

$$\tilde{\boldsymbol{d}}^{k+1} = \boldsymbol{d}^k + \Delta t \boldsymbol{v}^k + \frac{\Delta t^2}{2}(1-2\beta)\boldsymbol{a}^k, \tag{62}$$

$$\tilde{\boldsymbol{v}}^{k+1} = \boldsymbol{v}^k + (1-\gamma)\Delta t a^k, \tag{63}$$

$$(\boldsymbol{M} + \gamma\Delta t\boldsymbol{C} + \beta\Delta t^2\boldsymbol{K})\boldsymbol{a}^{k+1} = \boldsymbol{F}^{k+1} - \boldsymbol{C}\tilde{\boldsymbol{v}}^{k+1} - \boldsymbol{K}\tilde{\boldsymbol{d}}^{k+1}, \tag{64}$$

$$\boldsymbol{d}^{k+1} = \tilde{\boldsymbol{d}}^{k+1} + \beta\Delta t^2\boldsymbol{a}^{k+1}, \tag{65}$$

$$\boldsymbol{v}^{k+1} = \tilde{\boldsymbol{v}}^{k+1} + \gamma\Delta t\boldsymbol{a}^{k+1}. \tag{66}$$

In the above, $\boldsymbol{d}^k = \boldsymbol{\phi}(t_k)$, $\boldsymbol{v}^k = \dot{\boldsymbol{\phi}}(t_k)$, and $\boldsymbol{a}^k = \ddot{\boldsymbol{\phi}}(t_k)$. Any of the members of the Newmark family may be used, including the second-order accurate $\gamma = 1/2$, and unconditionally stable trapezoidal rule ($\beta = 1/4$), and conditionally stable central difference method ($\beta = 0$). When solving using the explicit central difference method, Eq. (64) may be decoupled using standard diagonal mass and damping matrices.

The solution of (64) requires that the forcing term $\boldsymbol{F}^{k+1}$, and therefore $\boldsymbol{z}_{nm}^{k+1}$ be available. The value $\boldsymbol{z}_{nm}^{k+1}$, may be computed concurrently using an explicit time-integrator applied to (15); e.g., the explicit second-order accurate Adams–Bashforth algorithm

$$\boldsymbol{z}_{nm}^{k+1} = \boldsymbol{z}_{nm}^{k} + \frac{\Delta t}{2}\left[\boldsymbol{A}_n(3\boldsymbol{z}_{nm}^{k} - \boldsymbol{z}_{nm}^{k-1}) + c\boldsymbol{e}_1(3\phi_{nm}(R,t_k) - \phi_{nm}(R,t_{k-1}))\right]. \tag{67}$$

3.2. Space-time discretization for the far-field

Let u_j^k denote the approximation of $u(r_j,t_k)$ where $r_j = R + j\Delta r$, and $t_k = k\Delta t$. Following the discretization used in [33], for each mode n, the radial wave Eq. (45) is approximated using the central difference operator for both $u_{,tt}$ and $u_{,rr}$ and with u, averaged about u_j^k

$$\frac{(u_j^{k+1} - 2u_j^k + u_j^{k-1})}{(c\Delta t)^2} = \frac{(u_{j+1}^k - 2u_j^k + u_{j-1}^k)}{(\Delta r)^2} - n(n+1)\frac{(u_{j+1}^k + 2u_j^k + u_{j-1}^k)}{(2r_j)^2}. \tag{68}$$

Using the method of characteristics, we set $\Delta r = c\Delta t$, so that (68) specializes to the explicit difference scheme,

$$u_j^{k+1} = u_{j+1}^k + u_{j-1}^k - u_j^{k-1} - n(n+1)\left(\frac{\Delta r}{2r_j}\right)^2(u_{j+1}^k + 2u_j^k + u_{j-1}^k). \tag{69}$$

For $n = 0$, the radial equation reduces to the 1D wave equation, and with $\Delta r = c\Delta t$, the discretization is exact. For $n \geqslant 1$, the discretization is second-order accurate for integrating forward in time and the approximation error grows as the mode number n increases.

The discrete energy associated with this discretization, for each mode, is [38]

$$E_k/\Delta r = \frac{1}{2}\sum_j\left(\frac{u_j^{k+1} - u_j^k}{c\Delta t}\right)^2 + \frac{1}{2}\sum_j\left(\frac{u_{j+1}^{k+1} - u_j^{k+1}}{\Delta r}\right)\left(\frac{u_{j+1}^k - u_j^k}{\Delta r}\right) + \frac{1}{2}n(n+1) \times \sum_j\left(\frac{u_{j+1}^{k+1} + u_j^{k+1}}{2r_j}\right)\left(\frac{u_{j+1}^k + u_j^k}{2r_j}\right). \tag{70}$$

If (68) is multiplied by $1/2(u_j^{k+1} - u_j^{k-1})$, the identity $E_k = E_{k-1}$ results. Thus $E_k = E_0$, for $k = 0,1,2,\ldots$, and the scheme appears to be stable. Other averaging schemes for u_j^k/r_j are possible; however, our numerical studies indicate that the averaging used in (68), is stable, and more accurate compared to the competing schemes.

To ensure outgoing waves, an infinite grid in the radial coordinate may be used as suggested in [33], such that reflected waves from the boundary do not influence the solution at the point of interest $R < r \leqslant R_0$, for times less than the final time. In this approach, a large radial grid of length of order $O(cT)$, where c is the wave speed and T is the final time is required. For moderate to large times, this approach results in large computer expense.

In this work, we truncate the exterior grid at the finite radius, $r_l = R + l\Delta r = R_0$, and impose the nonreflecting boundary condition (49). Using a simple difference formula for $u_{,r}$ and $u_{,t}$ centered at $j = l$, and setting $\Delta r = c\Delta t$ gives,

$$u_{l+1}^k = u_l^{k-1} - u_l^{k+1} + u_{l-1}^k - 2\Delta r(\boldsymbol{d}_n \cdot \boldsymbol{w}_{nm}^k). \tag{71}$$

Substituting (71) into (69) evaluated at $j = l$, and after rearranging, we obtain,

$$u_l^{k+1} = u_{l-1}^k - \frac{n(n+1)\Delta r^2}{8R_0^2 - n(n+1)\Delta r^2}\left(u_{l-1}^k + 2u_l^k + u_l^{k-1}\right) - 2\Delta r\left[1 - \frac{4R_0^2}{8R_0^2 - n(n+1)\Delta r^2}\right]\boldsymbol{d}_n \cdot \boldsymbol{w}_{nm}^k. \tag{72}$$

For $n = 0$, the boundary condition reduces to $B_1[u] = 0$, and the inner product $\boldsymbol{d}_0 \cdot \boldsymbol{w}_{om}^k$ is set to zero. We note a similar discretization may be used for the NRBC in the form (26), where $\boldsymbol{d}_n \cdot \boldsymbol{w}_{nm}^k$ is replaced by $-R_0\, v_{nm,1}^k$, where $v_{nm,1}^k$ is a solution to (28) at R_0 and time step t_k.

To update the solution on the boundary for modes $n \geqslant 1$, the values $\boldsymbol{w}_{nm}(t_k) = \boldsymbol{w}_{nm}^k$ are needed. To numerically solve (42), the second-order accurate, and the unconditionally stable, Adams–Moulton method (trapezoidal rule) may be used

$$\left(\boldsymbol{I} - \frac{\Delta r}{2c}\boldsymbol{B}_n\right)\boldsymbol{w}_{nm}^{k+1} = \left(B_m I + \frac{\Delta r}{2c}\boldsymbol{B}_n\right)\boldsymbol{w}_{nm}^k + \frac{\Delta r}{2}(\phi_{nm}(R_0, t_{k+1}) + \phi_{nm}(R_0, t_k))\boldsymbol{e}_1. \tag{73}$$

The computational work required in solving (73) is negligible, since the matrices $\boldsymbol{B}_n$, are relatively small (usually $N \leqslant 25$), and remain constant. For far-field points sufficiently distant from the source of radiation, such that $kR_0 \gg n^2 + 1$, the exact boundary condition may be simplified a-priori to the B_1 condition, i.e., $\boldsymbol{d}_0 \cdot \boldsymbol{w}_{0m}^k$ may be set to zero in (72).

3.3. Far-field computation

One approach for computing the far-field solution is to save the near-field solution on the artificial boundary Γ for later use. In this case, the computation would be performed in two stages. In the first, the near-field solution is computed, then, based on the solution on the artificial boundary, the far-field in the exterior region $\mathscr{D}$ may be computed as a *post-process*. A general approach would be to save the nodal solution $\boldsymbol{\phi}_\Gamma(t_k)$ on the Γ to disk at each time-step $t_1, t_2, \ldots, T$, then recompute the spherical harmonics $\phi_{nm}(R, t_k) = \boldsymbol{f}_{nm}^{*\mathrm{T}} \cdot \boldsymbol{\phi}_\Gamma(t_k)$ to drive the far-field solution. Alternatively, since the total number of harmonics $N_\mathrm{T} = N(N+1)$ included in the series expansion is generally less than the number of nodes on the artificial boundary, i.e., $N_\mathrm{T} \ll N_\Gamma$, the amount of computation and disk storage may be reduced by saving the modes $\phi_{nm}(R, t_k)$, $k = 1, 2, \ldots, K$, already computed from the near-field solution and the NRBC, instead of the entire nodal solution $\boldsymbol{\phi}_\Gamma(t)$ on the artificial boundary surface.

However, even with this reduction, for moderate to long time intervals $I = [0, T]$, the amount of disk storage and data transfer required for this two-stage process may become excessive. To address this problem, we show how to solve the far-field solution *concurrently* with the near-field solution and the NRBC. In this approach the modes $\phi_{nm}(R, t)$ are only computed as needed and stored in memory at time step t_k and the previous step t_{k-1}. The complete algorithm for computing the far-field solution concurrently with the near-field solution using Newmark's method and the NRBC defined in (11) is summarized below; a similar procedure is used for the direct application of the central difference method to (57). The implementation of (19) for the near-field, in conjunction with the far-field computation follows the same procedures described herein, with little modification:

1. (*Initialize near-field data*): Set $\boldsymbol{z}_{nm}^0 = \boldsymbol{z}_{nm}^{-1} = 0$; $\boldsymbol{d}^0 = \boldsymbol{\phi}(0)$ and $\boldsymbol{v}^0 = \dot{\boldsymbol{\phi}}(0)$, and calculate $\boldsymbol{a}^0 = \ddot{\boldsymbol{\phi}}(0)$ from $\boldsymbol{M}\boldsymbol{a}^0 = \boldsymbol{F}^0 - B_m C\boldsymbol{v}^0 - \boldsymbol{K}\boldsymbol{d}^0$, $\boldsymbol{d}^{-1} = \boldsymbol{d}^0 - \Delta t\boldsymbol{v}^0 + (\Delta t^2)/2\boldsymbol{a}^0$.
2. (*Initialize far-field data*): For each mode n, m, set $\boldsymbol{w}_{nm}^0 = 0$, and $u_j^0 = 0$, for all points r_j, $j = 1, \ldots, l$.

3. (*Compute the spherical harmonic transform*): Calculate $\phi_{nm}(R,t_k)$ and $\phi_{nm}(R,t_{k-1})$, from (61), and set $u_0^k = u(R,t_k) = R\phi_{nm}(R,t_k)$.
4. (*Update near-field solution*): Compute $\boldsymbol{z}_{nm}^{k+1}$ using (67); predict $\tilde{\boldsymbol{d}}^{k+1}$ and $\tilde{\boldsymbol{v}}^{k+1}$ from (62) and (63); Calculate $\boldsymbol{a}^{k+1}$ from (64); update $\boldsymbol{d}^{k+1}$ and $\boldsymbol{v}^{k+1}$ using (65) and (66).
5. (*Update far-field data*): Compute $\boldsymbol{w}_{nm}^{k}$ using (73); for each mode, update u_j^{k+1} using (69) for $j = 1,\ldots,l-1$ and (72) for $j = l$.
6. (*Compute the spherical harmonic expansion*): Evaluate the far-field solution for specified points (r_j,θ,φ), in the range $R < r_j \leqslant R_0$, using (35).
7. Increment the time step from k to $k+1$, Go back to step 3.

4. Numerical studies

4.1. Far-field calculation for individual modes

In this first study, numerical examples are performed to assess the accuracy of the finite difference approximation (69) in integration of the radial wave equation for individual modes $\phi_{nm}(r,t)$. The accuracy of the approximate operator B_1 and the nonreflecting boundary condition NR1 applied to the far-field boundary are also compared for each mode. Both time-harmonic and transient radiation are studied.

4.1.1. Time-harmonic radiation

Consider time-harmonic radiation for radial modes $u(r,t) = r\phi_{nm}(r,t)$, such that at $R = 1.25$,

$$\phi_{nm}(R,t) = \sin\omega t, \quad t \geqslant 0. \tag{74}$$

The exact steady-state solution to the radial wave equation for this input is,

$$\phi_{nm}(r,t) = -\mathrm{Imag}\left\{ \frac{h_n(kr)}{h_n(kR)} \mathrm{e}^{-\mathrm{i}\omega t} \right\}, \quad r \geqslant R, \;\; t \geqslant 0. \tag{75}$$

In the above, h_n are spherical Hankel functions of the first kind and $k = \omega/c$ is the wave number. For $n = 0$, $h_0(kr)$ is a simple exponential function, so that

$$\phi_{0m}(r,t) = \mathrm{Imag}\left\{ \frac{i}{h_n(kR)} \mathrm{e}^{\mathrm{i}(kr-\omega t)} \right\} \frac{1}{kr}. \tag{76}$$

For this mode, $B_1[\phi_{0m}] = 0$, and the exact nonreflecting boundary condition NR1 reduces to the local B_1 operator. In addition, for $n = 0$, the wave equation reduces to the 1D wave equation, and the time-integration scheme given in (69) with $\Delta r = c\Delta t$ is exact.

Using the large-argument asymptotic expansion for $h_n(kr)$, in the limit $kr \gg n^2 + 1$, we have,

$$\phi_{nm}^{\infty}(r,t) = -\mathrm{Imag}\left\{ \frac{1}{h_n(kR)} \mathrm{e}^{\mathrm{i}(kr-\omega t-\frac{\pi}{2}(n+1))} \right\} \frac{1}{kr}. \tag{77}$$

In the asymptotic limit, the solution (77) satisfies $B_1[\phi_{nm}^{\infty}] = 0$.

For numerical solutions, we set the frequency $\omega = 4\pi$, wave speed $c = 1$, and time step $\Delta t = 0.005$. Fig. 2 shows time-dependent solutions using NR1, and B_1 at the far-field truncation point at $R_0/R = 2$, compared to the exact steady-state solution. Results are shown for three increasingly higher modes: $n = 0, 10, 20$. For $n = 0$, the finite difference approximation (69) and boundary conditions are exact. With this frequency and radial observation point, the normalized wave number is $kr = 10$, and solutions using B_1 are accurate only for $n < 3$. Numerical results for modes $n = 10$ and $n = 20$ using B_1, exhibit significant error in both amplitude and phase at steady state, while the NR1 solution matches the exact solution very well for both $n = 10$ and $n = 20$.

Fig. 3 compares the relative error in steady-state amplitude vs mode n for results obtained using NR1 positioned at $R_0 = 2.5$, and B_1 positioned at $R_0 = 2.5, 5$ and 15. Results are also given for an "infinite mesh" solution, denoted (IM), obtained by extending the radial discretization to a distant point such that outgoing

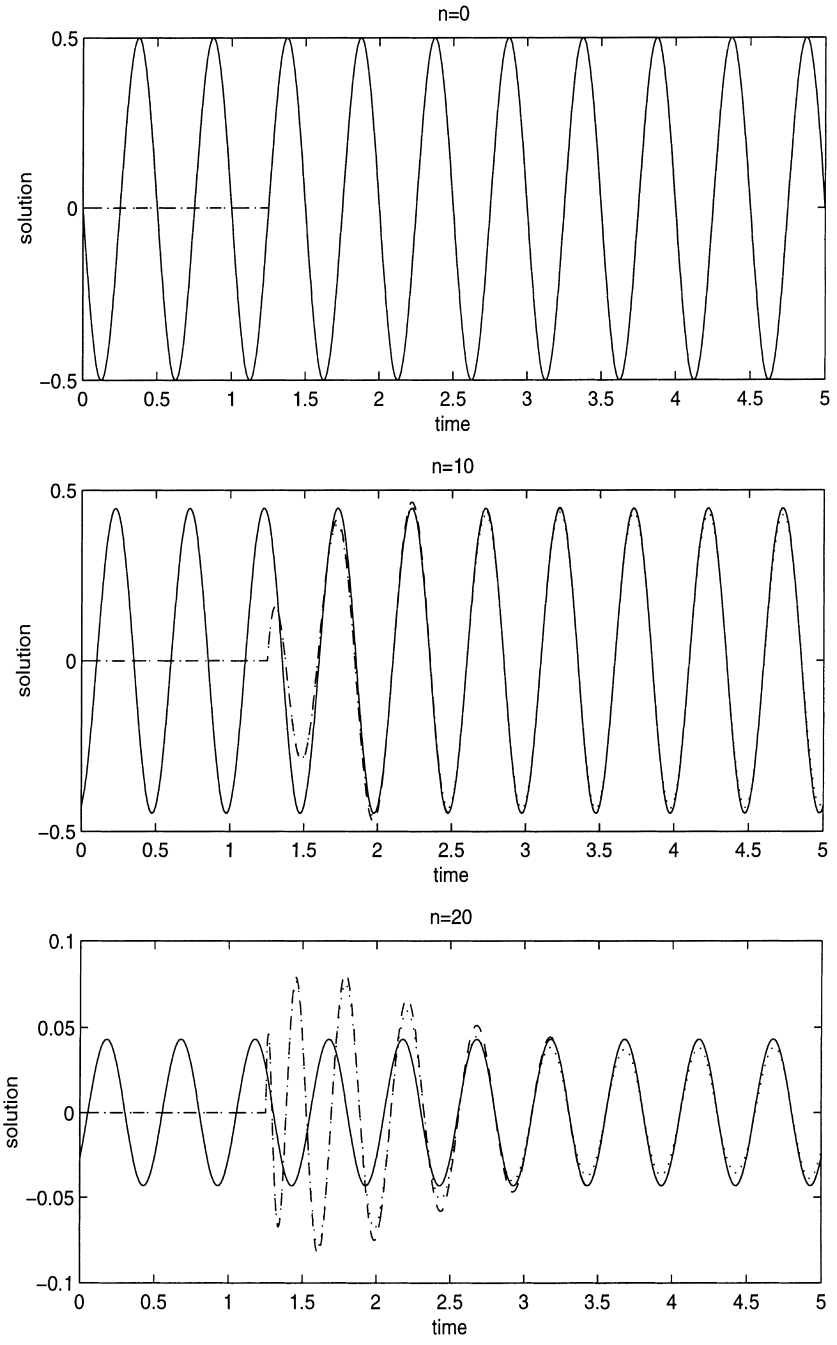

Fig. 2. Time-dependent solutions for modes $n = 0, 10$ and 20, computed using NR1 and B_1 compared to the exact steady-state solution at $kR_0 = 10$. Solid lines denote exact steady-state solution; Dashed lines denote NR1; Dotted lines denote B_1.

waves with speed $c = 1$ do not reach the far-field truncation boundary in the time-interval of interest. The error in the IM solution is caused purely by the finite difference approximation (69) of the radial wave equation. As expected, discretization error for the IM solution generally increases with n. The error for $n \leqslant 20$ are all less than 0.4%, which indicate the high accuracy of the finite difference approximation (69) for the current time step. The error in the B_1 solution decreases, as expected, when the truncation boundary is moved from $R_0 = 2.5$ to 15. With the calculation truncated at $R_0 = 2.5$, the NR1 gives very accurate results with error only slightly higher than the IM solution.

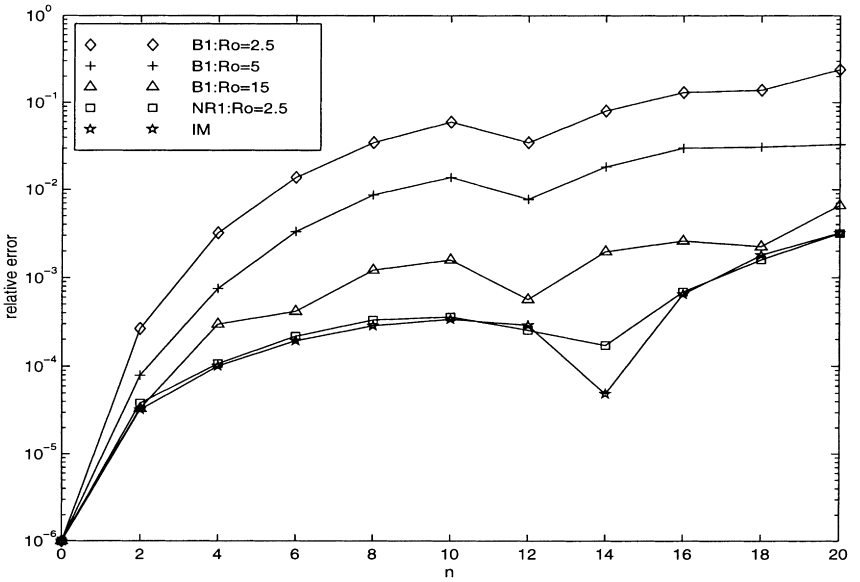

Fig. 3. Relative amplitude error vs mode n at $r = 2.5$. Results are computed using B_1 with truncation boundary at $R_0 = 2.5, 5$, and 15; NR1 at $R_0 = 2.5$; and IM.

4.1.2. Transient radiation

Consider a pulse at $R = 1.25$ described by

$$\phi_{nm}(R,t) = te^{-bt}, \quad t \geqslant 0, \tag{78}$$

where $b = 4$ controls the pulse width. The exact solution for the first two radial modes are obtained by Laplace transform, with the result

$$\phi_{0m}(r,t) = (R/r)\tau e^{-b\tau}\mathrm{H}(\tau), \tag{79}$$

$$\phi_{1m}(r,t) = (R/r)^2\left\{\left[e^{-b\tau} - e^{-\frac{c}{R}\tau}\right](r-R)/(c-bR)^2 + \tau e^{-b\tau}(br-c)/(bR-c)\right\}\mathrm{H}(\tau). \tag{80}$$

In the above, $H(\cdot)$ is the Heaviside step function and $\tau = t - (r-R)/c$.

Fig. 4 compares the transient solutions for modes $n = 0$ and $n = 1$ obtained using NR1 and B_1, with truncation boundary set at $R_0 = 2.5$. As discussed earlier, for mode $n = 0$ NR1 coincides with B_1 which is exact for the mode $n = 0$. The solutions obtained using NR1 and B_1 are observed to match the exact solution perfectly for $n = 0$. For $n = 1$, the B_1 solution captures the early time solution accurately yet exhibits significant error during the tail end of the pulse. In contrast, the NR1 solution cannot be distinguished from the exact solution.

4.2. Transient radiation from piston on a sphere

We next consider axisymmetric radiation from a circular piston on a sphere with radius $a = 0.5$. The piston is represented by,

$$\phi(a,\theta,t) = f(\theta)\sin\omega t\, H(t), \tag{81}$$

where $H(t)$ is the unit-step (Heaviside) function and,

$$f(\theta) = \begin{cases} 1, & 0^\circ \leqslant \theta \leqslant 15^\circ \\ \dfrac{\cos\theta - \cos 30^\circ}{\cos 15^\circ - \cos 30^\circ}, & 15^\circ < \theta \leqslant 30^\circ \\ 0 & \text{otherwise.} \end{cases} \tag{82}$$

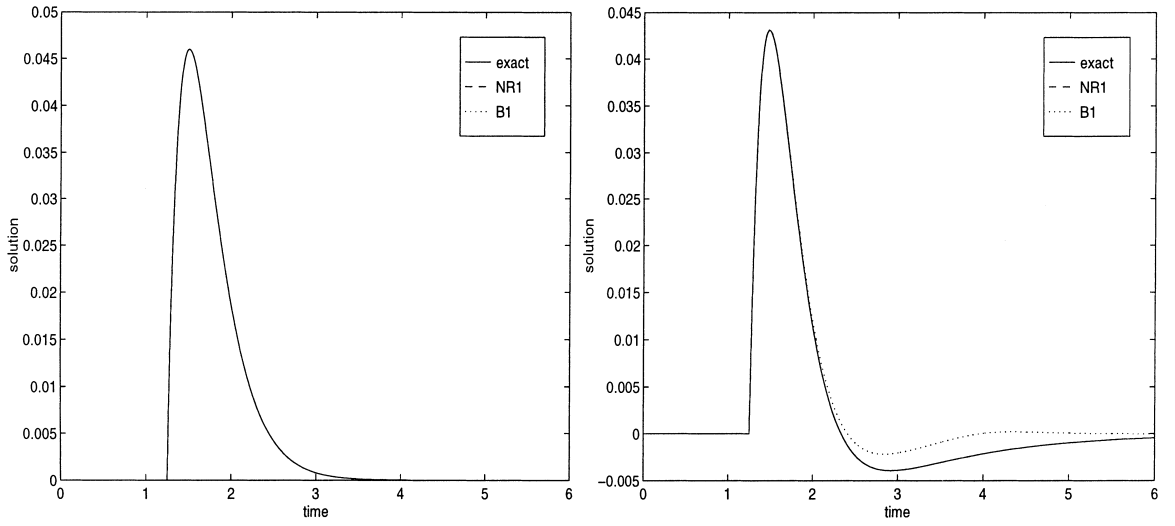

Fig. 4. Transient solutions at $r = 2.5$ obtained using NR1, B_1 and analytic solution. (Left) $n = 0$. (Right) $n = 1$.

This problem is chosen since an exact solution is available and it is sufficient to study the accuracy of far-field computations for a problem involving an infinite number of spherical harmonics. The problem is challenging in that the waves radiated at the piston pole $\theta = 0°$ are attenuated by a geometric spreading loss as they travel along longitudes down to the south pole $\theta = 180°$. In the region opposite the piston (shadow zone), the amplitude of the waves are significantly lower than near the piston, [39]. The exact transient solution to this problem contains a term decreasing rapidly with time, which can be explained due to the presence of "creeping waves", i.e., the radiation from the piston can encircle the sphere a number of times, so that the transient solution in principle never reaches a steady-state, although in practice the exponentially decreasing term quickly becomes negligible as time increases.

The problem is axisymmetric and independent of φ. The exact steady-state solution to this problem is obtained by expanding the function $f(\theta)$ as a series of Legendre functions P_n, and evaluating the radiated solution at $r = a$, with the result,

$$\phi(r,\theta,t) = -\mathrm{Imag}\left\{ \mathrm{e}^{-\mathrm{i}\omega t} \sum_{n=0}^{\infty} A_n \frac{h_n(kr)}{h_n(ka)} P_n(\cos\theta) \right\} \tag{83}$$

with coefficients,

$$A_0 = \frac{1}{4}(2 - \cos 15° - \cos 30°) \tag{84}$$

and for $n = 1, 2, \ldots,$

$$A_n = \frac{1}{2}[P_{n-1}(\cos 15°) - P_{n+1}(\cos 15°)] + \frac{2n+1}{2} \int_{\cos 30°}^{\cos 15°} \frac{u - \cos 30°}{\cos 15° - \cos 30°} P_n(u)\, \mathrm{d}u,$$

where $u = \cos\theta$. In the above, the integral is evaluated exactly using $n/2 + 1$ Gaussian quadrature points.

Since the problem is independent of φ, it is sufficient to compute the near-field solution in the domain Ω defined by the (r, θ) plane for $a \leqslant r \leqslant R$, and $0 \leqslant \theta \leqslant \pi$. The near-field is discretized with a uniform mesh of standard four-node bilinear axisymmetric finite elements. The mesh is defined with 20×240 elements and a near-field truncation boundary set at $R = 0.75$, (20 evenly spaced elements in $0.5 \leqslant r \leqslant 0.75$, and 240 evenly spaced elements in $0 \leqslant \theta \leqslant \pi$), see Fig. 5.

For all calculations, the far-field solution is computed concurrently with the near-field solution using the nonreflecting boundary condition NR1(N) with $N = 20$ applied on Γ, and $\Delta r = c\Delta t$. The computation is driven from rest to steady-state with a normalized frequency $\omega a/c = \pi$ and a time step $\Delta t = 0.005$.

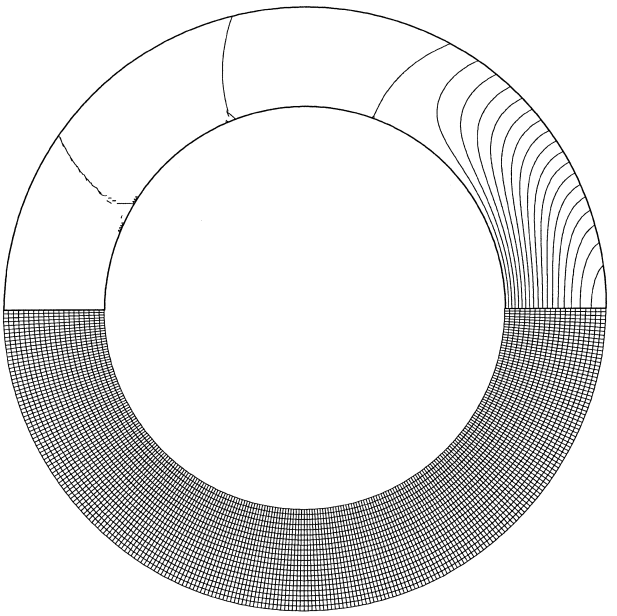

Fig. 5. (Top) Near-field solution contours at $t = 14$, using NR1 (20) for radiating piston on sphere problem driven at $ka = \pi$. (Bottom) Finite element discretization. Mesh consists of 20×240 evenly spaced four-node axisymmetric elements over $0.5 \leqslant r \leqslant 0.75$, and $0 \leqslant \theta \leqslant \pi$.

Fig. 5 shows contours of the near-field solution using NR1 (20). The far-field solution at observation points defined with coordinates $r/a = 2$ and $\theta = 0, 90°$ and 180° are shown in Fig. 6. Time-histories are compared using the local B_1 operator positioned at the far-field points $\hat{R}_0 = R_0/a = 2, 4, 12$, and NR1 at $\hat{R}_0 = 2$. Fig. 6 also shows the instantaneous error on a sphere with radius $r_0/a = 2$, during the steady-state time interval $15 < t < 20$. The instantaneous error $e(t) = \phi^h(t) - \phi(t)$, measured in L_2 norm is defined as,

$$E(t) = \left\{ \int_0^{\pi} \left[\phi^h(r_0, \theta, t) - \phi(r_0, \theta, t)\right]^2 \sin\theta \, \mathrm{d}\theta \right\}^{1/2}, \tag{85}$$

where ϕ^h is the numerical solution with nonreflecting boundary and ϕ is the exact steady-state solution.

Directly in front of the piston at $\theta = 0$, the far-field solution using the local B_1 operator shows a slight phase and amplitude error when placed at $\hat{R}_0 = 2$. Accuracy is improved by moving the far-field boundary to positions $\hat{R}_0 = 4, 12$. At these more distant points, the solution can barely be distinguished from the exact steady-state solution. As the observation point is moved around the sphere to $\theta = \pi/2$, solutions using B_1 positioned at both $\hat{R}_0 = 2$ and $\hat{R}_0 = 4$, show large phase and amplitude errors. In this case, the local B_1 operator must be moved to the distant point $\hat{R}_0 = 12$ to obtain accurate solutions. In the difficult shadow zone on the backside of the piston, the solution using B_1 exhibits spurious reflections, even when the far-field boundary is moved to $\hat{R}_0 = 12$. The solution obtained using NR1 matches the exact solution at all observation points as expected. The error $E(t)$ using the nonreflecting boundary condition NR1 is reduced by an order of magnitude compared to the local B_1 boundary condition applied at points $\hat{R}_0 \leqslant 4$. Only by moving the B_1 operator to far-field points $\hat{R}_0 > 12$ does the accuracy approach that of NR1.

4.3. Transient scattering of a plane wave by a sphere

Another common application involving an infinite number of harmonics is the problem of scattering of an incident wave. For a model problem with an exact solution, we consider a sphere of radius $a = 1$ on which we assume a homogeneous Dirichlet boundary condition,

$$\phi = 0 \quad \text{on } \|\boldsymbol{x}\| = a. \tag{86}$$

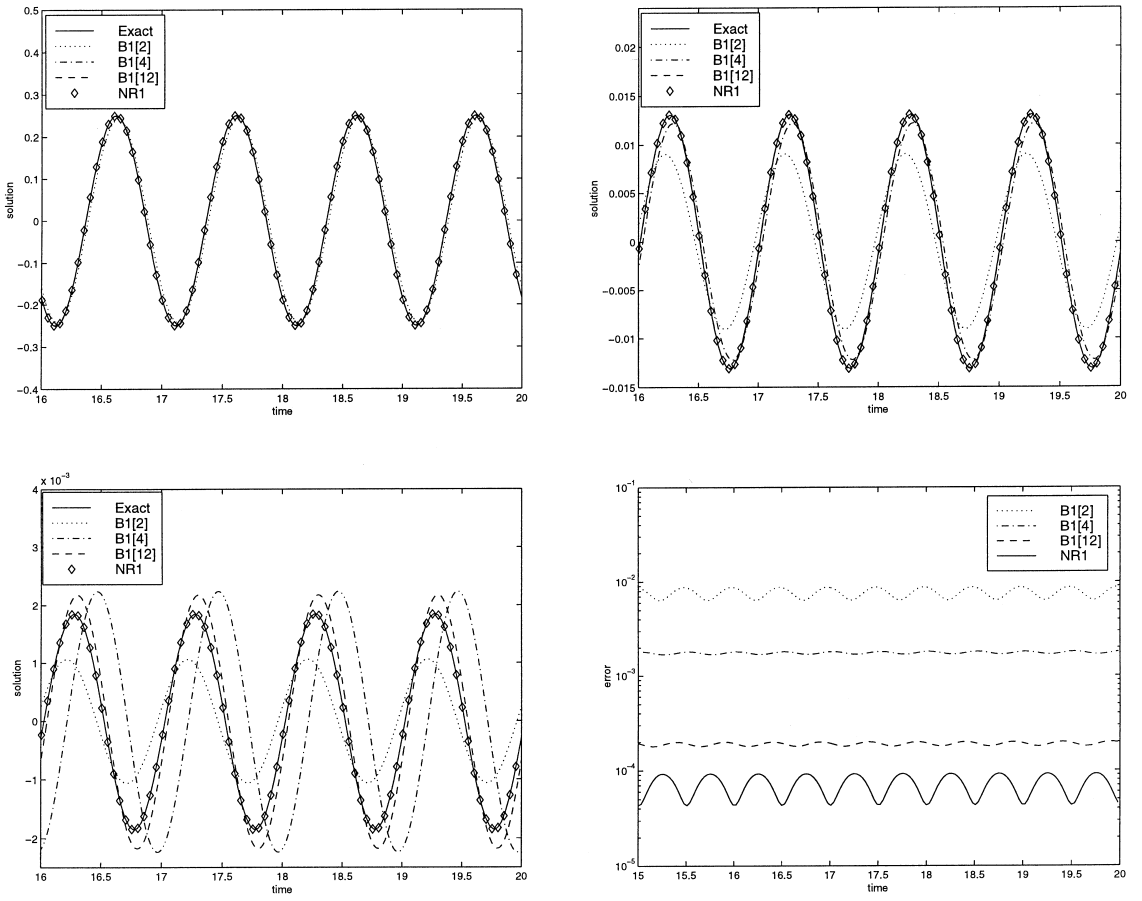

Fig. 6. Time-histories at observation points at $R_0/a = 2$, and (top-left) $\theta = 0$, (top-right) $\theta = \pi/2$, (bottom-left) $\theta = \pi$. (Bottom-right) Instantaneous error $E(t)$ at steady-state. Results compared for local operator $B_1[R_0/a]$, at $R_0/a = 2, 4, 6, 12$ and NR1 at $R_0/a = 2$.

Let the incident wave be a traveling plane wave along the x-axis at speed c, i.e.,

$$\phi_{\mathrm{i}} = \begin{cases} \sin[k(x - x_0) - \omega t], & t \geqslant \frac{x - x_0}{c}, \\ 0, & t < \frac{x - x_0}{c}. \end{cases} \tag{87}$$

Here the wave is incident from the $\theta = \pi$ direction, and x_0 is the location of the plane wave at time $t = 0$. The total field $\phi(\boldsymbol{x}, t)$ is composed of a superposition of the incident wave $\phi_{\mathrm{i}}(x, t)$ and a scattered wave $\phi_{\mathrm{s}}(\boldsymbol{x}, t)$, i.e., $\phi = \phi_{\mathrm{i}} + \phi_{\mathrm{s}}$. With the Dirichlet boundary condition (86), the scattered field is a solution to the wave equation subject to the boundary condition,

$$\phi_{\mathrm{s}} = -\phi_{\mathrm{i}} = -\sin[k(x - x_0) - \omega t] H\left(t - \frac{x - x_0}{c}\right), \quad \text{on } \|\boldsymbol{x}\| = a. \tag{88}$$

The exact steady-state solution is obtained by setting $x = r\cos\theta$ and expanding the exponential form of the incident wave in spherical harmonics by means of an addition theorem [39]. For ϕ_{i} given in (87), the steady-state analytical solution is,

$$\phi_{\mathrm{s}} = \mathrm{Imag}\left\{ \mathrm{e}^{-\mathrm{i}(kx_0 + \omega t)} f(r, \theta) \right\}, \tag{89}$$

where

$$f(r, \theta) = \sum_{n=0}^{\infty} i^n (2n + 1) \frac{j_n(ka)}{h_n(ka)} h_n(kr) P_n(\cos\theta). \tag{90}$$

In the above, j_n and h_n are spherical Bessel's and Hankel's functions of the first kind, respectively.

The near-field is discretized with a uniform mesh of standard four-node bilinear axisymmetric finite elements (20 evenly spaced elements in $1.0 \leqslant r \leqslant 1.5$, and 240 evenly spaced elements in $0 \leqslant \theta \leqslant \pi$). The computation is driven from rest to steady-state with a normalized frequency $\omega a/c = \pi$ and a time step $\Delta t = 0.01$. The far-field solution is computed concurrently with the near-field solution using the nonreflecting boundary condition NR1 (20) on Γ, and $\Delta r = c\Delta t$.

Contours for the near-field solution computed using NR1(20) are shown in Fig. 7. Fig. 8 shows time-histories of near-field scattering on the artificial boundary Γ, at $\theta = 0$, and the backscattered point $\theta = \pi$. Results are compared using the local operators B_1, B_2 and $NR1$ (20) applied to the artificial boundary, with the exact solution. At the backscattered point, the solutions using B_2 and $NR1$ (20) can barely be distinguished with the exact solution after steady-state has been reached. Results for B_1 show small errors in amplitude and phase. However, on the other side of the sphere, at point $\theta = 0$, both operators B_1 and B_2 exhibit significant spurious reflection. As expected, the solution using NR1 (20) matched the exact solution very well.

The far-field solution at the observation point $r/a = 2$ and $\theta = 0$ is shown in Fig. 9. The far-field solution is computed based on the near-field solution obtained from NR1 (20) at $R/a = 1.5$. Far-field results are compared using the local B_1 operator positioned at positions $\hat{R}_0 = 2, 4, 12$, and NR1 at $\hat{R}_0 = 2$. At $\theta = 0$, the far-field solution using the local B_1 operator positioned at both $\hat{R}_0 = 2$ and $\hat{R}_0 = 4$, show significant phase and amplitude errors. As the far-field boundary is moved to the distant position $\hat{R}_0 = 12$ the solution can barely be distinguished from the exact steady-state solution. The solution obtained using NR1 matches the exact solution as expected. The L_2 error $E(t)$ using NR1 is reduced by an order of magnitude compared to B_1 applied at points $\hat{R}_0 \leqslant 4$. The accuracy of B_1 approaches that of NR1 when $\hat{R}_0 > 12$.

4.4. Transient radiation from a piston in infinite planar baffle

To study the accuracy of the far-field solution for a problem with an exact transient solution, we consider a circular piston of radius $a = 1$ embedded in a rigid infinite planar baffle moving with a uniform velocity in the normal direction. The velocity of the piston is specified to be a finite-duration modified Ricker [40] pulse

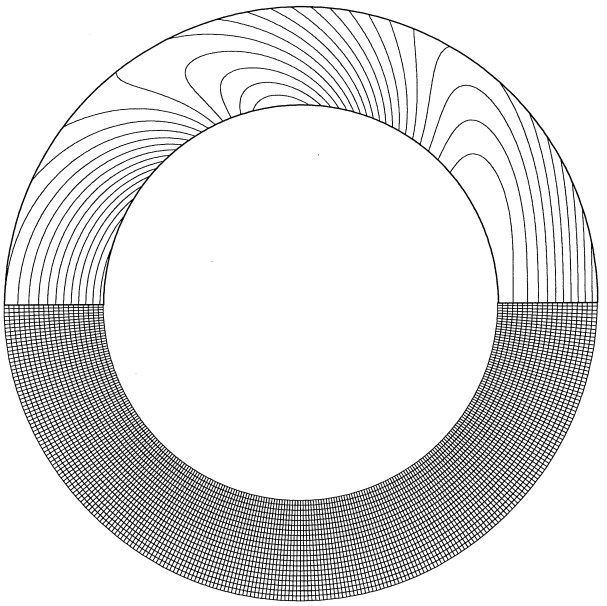

Fig. 7. ((Top) Near-field solution contours at $t = 28$, using NR1 (20) for scattering from a sphere with wave incident from the ($\theta = \pi$) direction, and normalized frequency $\omega a/c = \pi$. (Bottom) Finite element discretization consists of 20×240 evenly spaced four-node axisymmetric elements over $1.0 \leqslant r \leqslant 1.5$, and $0 \leqslant \theta \leqslant \pi$.

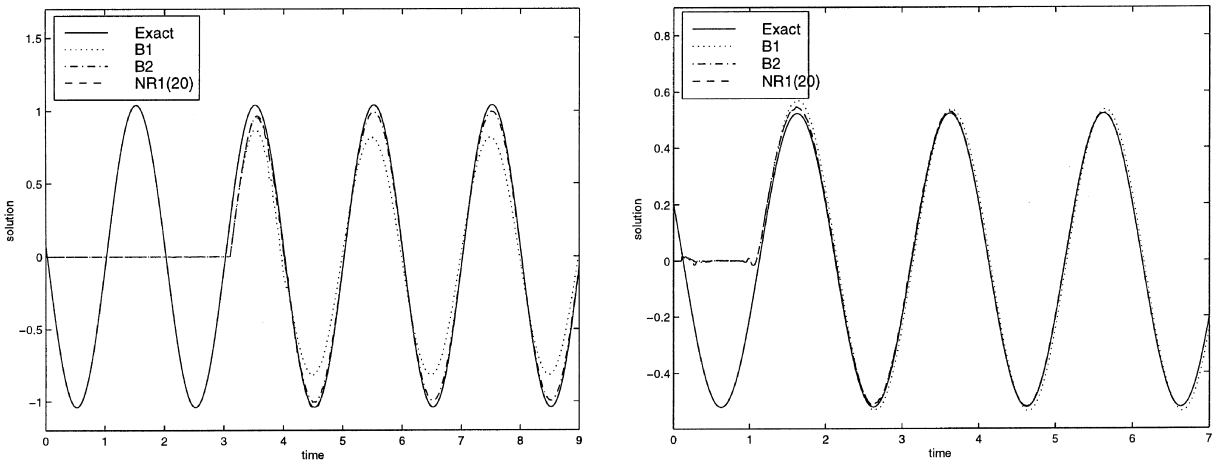

Fig. 8. Time-histories of near-field scattering on the artificial boundary Γ, at (left) $\theta = 0$, and (right) backscattered point $\theta = \pi$. Results compared for local operators B_1, B_2 and $NR1$ (N) with $N = 20$.

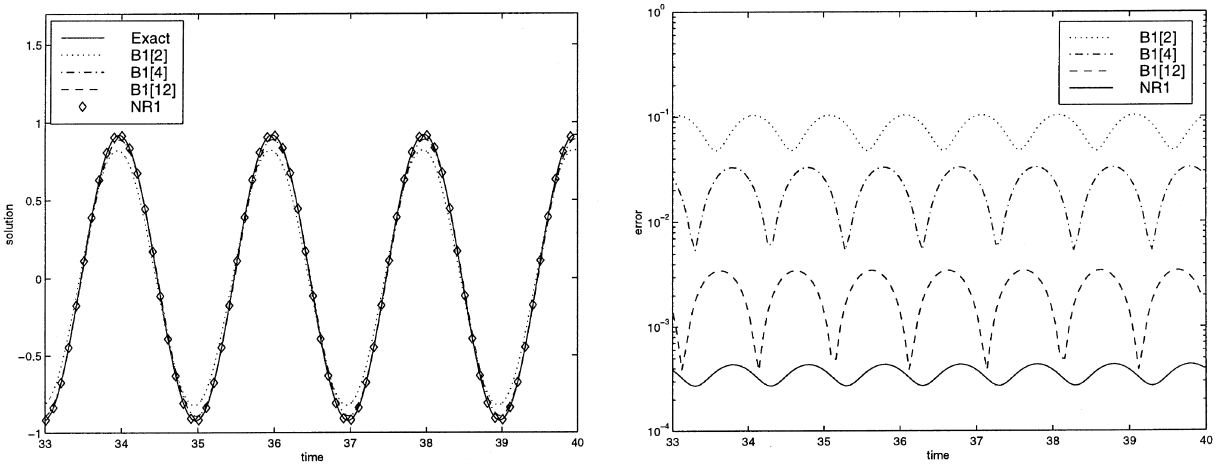

Fig. 9. Far-field scattering at $\omega a/c = \pi$. (Left) Time-history at far-field observation point $r/a = 2$. (Right) Instantaneous error $E(t)$ at steady-state. Results compared for operator $B_1[R_0/a]$ positioned at $R_0/a = 2, 4, 12$, and NR1 at $R_0/a = 2$.

$$v(t) = \begin{cases} \dfrac{(0.25u^2 - 0.5)\mathrm{e}^{-0.25u^2} - 13\mathrm{e}^{-13.5}}{0.5 + 13\mathrm{e}^{-13.5}} & \text{when } 0 \leqslant t \leqslant \dfrac{6\sqrt{6}}{\omega_r}, \\ 0 & \text{otherwise.} \end{cases} \tag{91}$$

In the above, $u = \omega_r t - 3\sqrt{6}$ where ω_r is the dominant frequency of the excitation. Fig. 10 shows the modified Ricker pulse and the amplitude of its Fourier transform. The Ricker pulse has the property that its Fourier transform has a single well-defined central frequency ω_r and has non-zero values only over a narrow frequency band. With this wavelet, we are able to excite a well-defined range of frequencies.

Let ϕ denote acoustic pressure, then the sound pressure field is determined by the wave equation and by the boundary conditions,

$$\frac{\partial \phi}{\partial z} = \begin{cases} -\rho_0 \dot{v}(t) & \text{on piston } \mathrm{P} = \{0 \leqslant r \leqslant a, \theta = \pi/2\}, \\ 0 & \text{on baffle } \mathrm{B} = \{r > a, \theta = \pi/2\}, \end{cases} \tag{92}$$

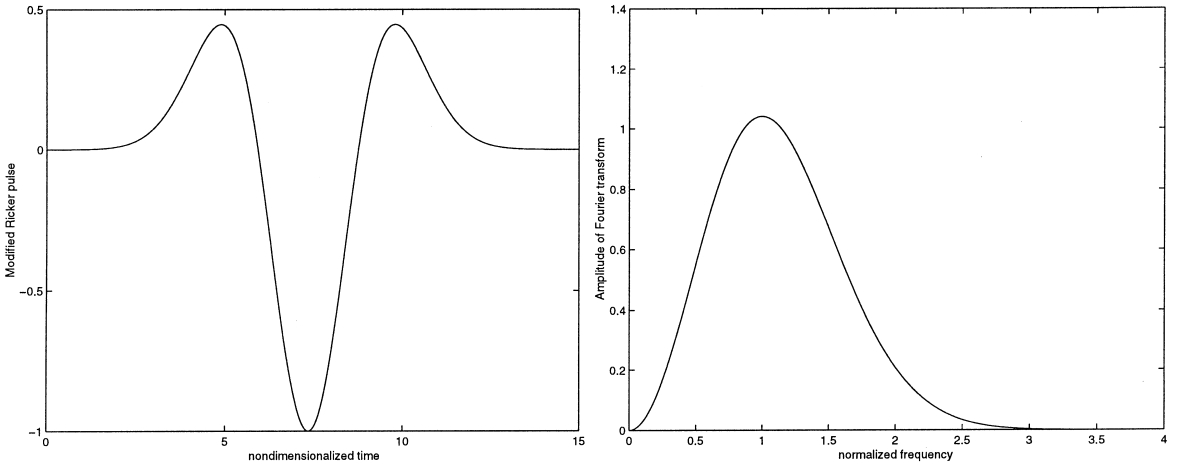

Fig. 10. Modified Ricker pulse and its Fourier transform. (Left) Pulse vs normalized time $\omega_r t$. (Right) The amplitude spectrum vs frequency ω/ω_r.

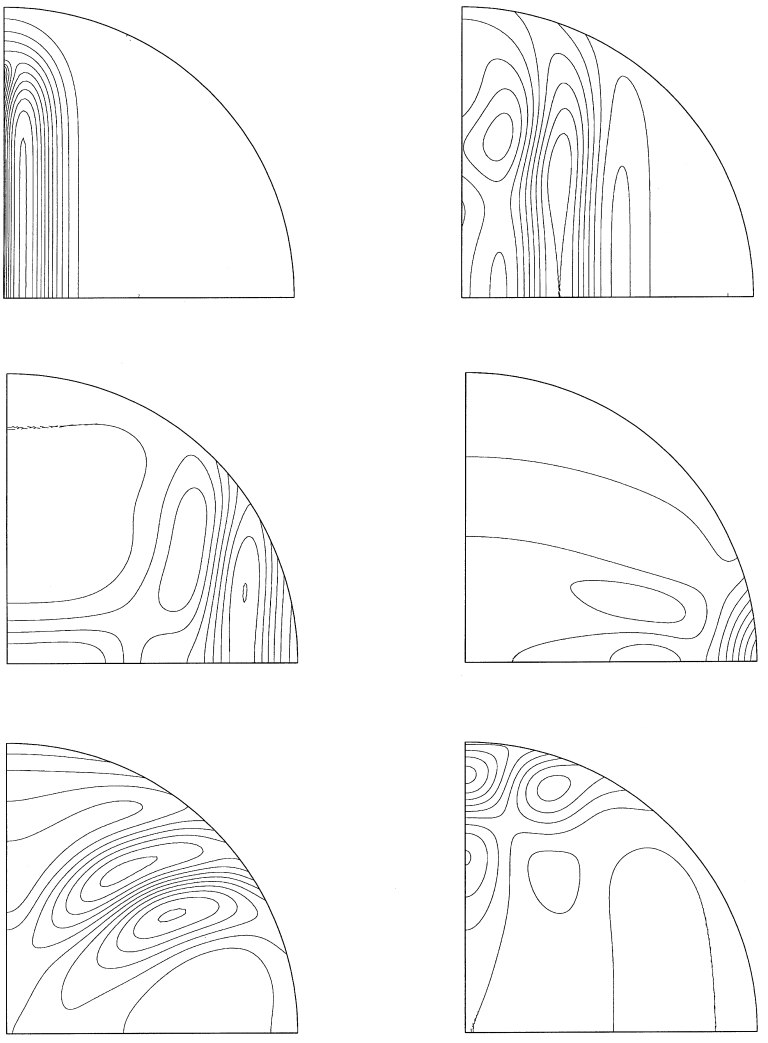

Fig. 11. Solution contours of NR1 (25) for transient radiation from circular piston in infinite planar baffle. (top-left): $t = 0.6$ s; (top-right): $t = 1.2$ s; (middle-left): $t = 1.8$ s; (middle-right): $t = 2.4$ s; (bottom-left): $t = 3.0$ s; (bottom-right): $t = 3.6$ s.

where z is the coordinate normal to the piston and baffle, $v(t)$ is the velocity of the piston, and a superimposed dot denotes a time derivative.

The solution $\phi(r,\theta,t)$ is rotationally symmetric about the z-axis normal to the center of the piston. Since the problem is axisymmetric, it is convenient to introduce cylindrical coordinates (ρ,z), where $\rho=\sqrt{x^2+y^2}$ is the polar radius (distance off the axis) of the circular piston. The analytic solution to this problem is obtained by means of an impulse response function $h(\rho,z,t)$ which is derived by Stepanishen [41] for a circular piston

$$\phi(\rho,z,t)=-\rho_0\frac{\partial}{\partial t}[v(t)*h(\rho,z,t)], \tag{93}$$

where ρ_0 is the density of the medium, and the asterisk is used to denote convolution in time. For observation points on the z-axis, the time convolution may be evaluated in closed-form. Points off-axis are integrated numerically. For this input, the solution on the z-axis consists of two Ricker pulses of opposite amplitude. The time delay of the initial pulse corresponds to the propagation time from the center of the piston to the spatial point, and the time delay of the second pulse corresponds to the propagation time from the edge of the piston to the spatial point.

For this semi-infinite problem, the truncation boundary Γ, for the near-field solution, is a semi-sphere in 3D. For a half-plane modeled as a rigid baffle, the sum on the indices in the spherical harmonic expansion

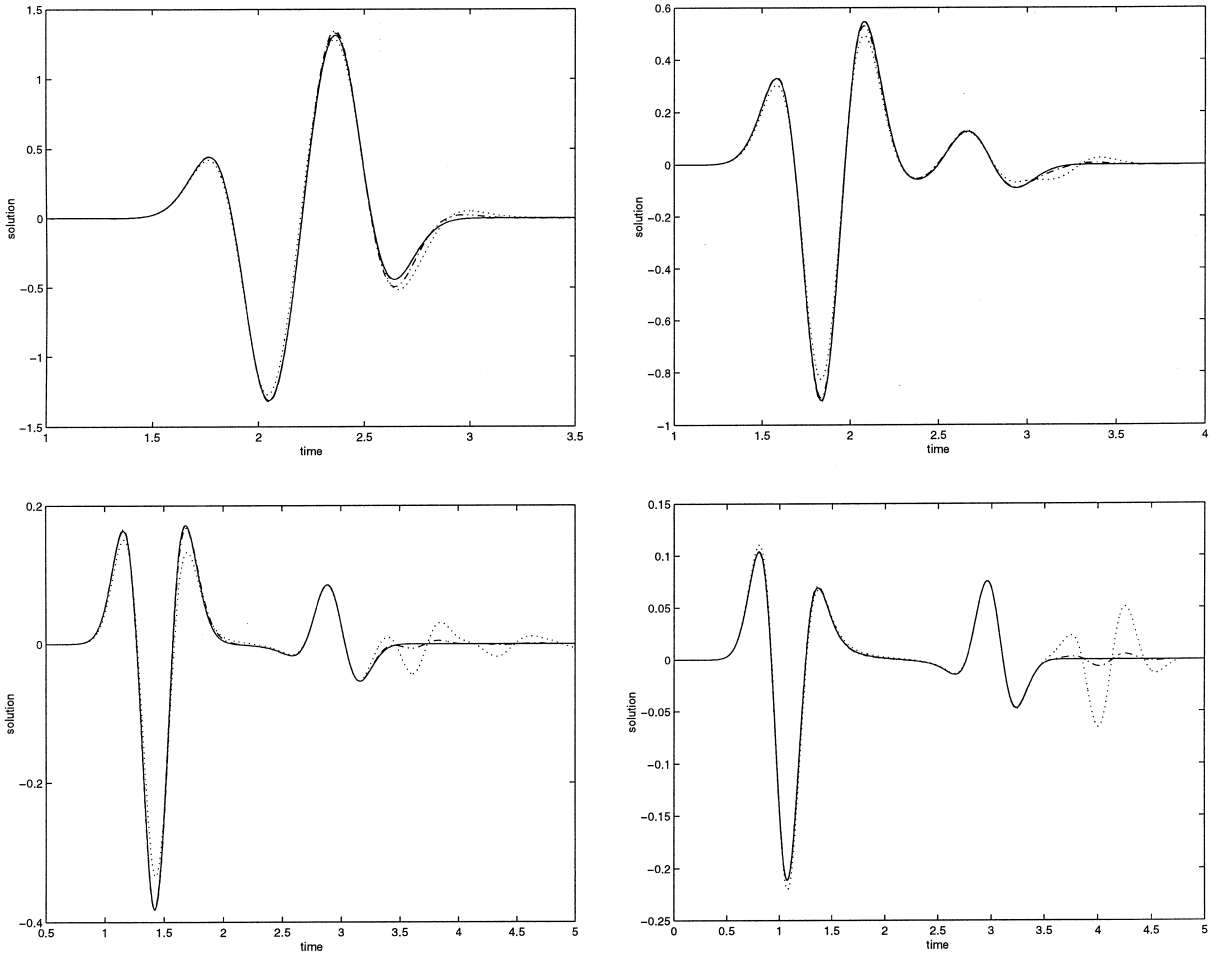

Fig. 12. Near-field solution at truncation boundary Γ for radiation from circular piston in infinite baffle. Time-histories at (top-left) $\theta=0$, (top-right) $\theta=30°$, (bottom-left) $\theta=60°$, (bottom-right) $\theta=90°$. Solid lines denote analytic solution; dashed lines denote NR1 (25); Dash–dotted lines denote B_2; Dotted lines denote B_1.

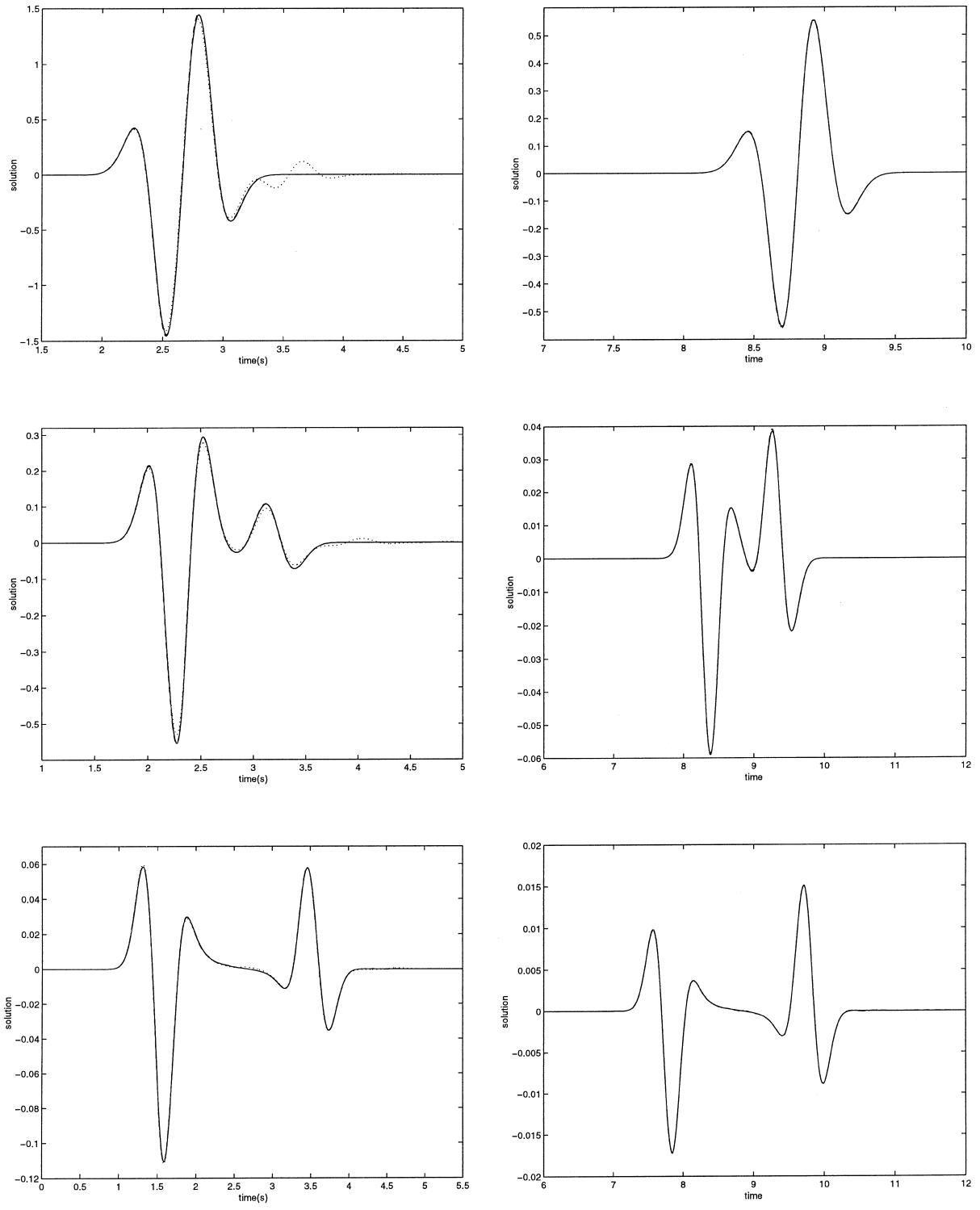

Fig. 13. Far-field solution for radiation from piston in infinite baffle. Time-histories at (left): $r = 1.75$, and (right): $r = 8$, and angles (top) $\theta = 0°$, (middle) $\theta = 30°$, (bottom) $\theta = 90°$. Solid lines denote analytic solution; dashed lines denote NR1; dotted lines denote B_1.

appearing in the NRBC are restricted to $n+m=$ even, and the transform is modified by a factor of two, with integration over the semi-sphere, i.e.,

$$\phi_{nm}(r,t) = 2\int_0^{2\pi}\int_0^{\pi/2} Y^*_{nm}(\theta,\varphi)\phi(r,\theta,\varphi,t)\sin\theta\,\mathrm{d}\theta\,\mathrm{d}\varphi, \quad n+m=\text{even}. \tag{94}$$

In this study, the frequency $\omega_r = 3\pi$ is used with a time step $\Delta t = 0.003$. The truncation boundary Γ is positioned close to the radius of the piston at $R/a = 1.25$. The finite element mesh consists of 150 evenly spaced elements along the z-axis from $0 \leqslant z \leqslant 1.25$, and 90 evenly spaced elements from $0 < \theta \leqslant \pi/2$.

Fig. 11 shows contours of the near-field solution using NR1 (25) on Γ at several time steps. Fig. 12 shows the near-field results at four discrete points on the truncation boundary $R = 1.25$. The results obtained using the local boundary conditions B_1, B_2 and non-reflecting boundary condition NR1 (25) are compared to the analytic solution. The NR1 (25) solution is observed to match the analytic solution at all points; the B_2 solution exhibits significant error at the trailing end of the second pulse, while B_1 causes significant spurious reflections during both the initial and secondary pulses. These results again demonstrate the high-accuracy achieved by the nonreflecting boundary condition compared to approximate operators.

The far-field solution is computed based on the near-field solution obtained from NR1 (25) at $R = 1.25$. The far-field solutions at observation points $r_1 = 1.75$ and $r_2 = 8$ are shown in Fig. 13 at three different angles $\theta = 0°, 30°$, and $90°$. These results are obtained using NR1 and B_1 with the far field truncated at $R_0 = r_1$ and $R_0 = r_2$, respectively. It is observed that the NR1 solution matches the analytic solution well at all points. The B_1 solution shows significant errors when positioned at $r_1 = 1.75$. However, when the far-field truncation boundary is moved further away from the radiating piston to position $r_2 = 8$, the B_1 local operator asymptotically approaches the exact nonreflecting boundary condition, and accurate solutions are obtained.

5. Conclusions

By exploiting the separable coordinate system outside a spherical artificial boundary, we pose an efficient method for accurately computing far-field solutions directly in the time-domain. At each discrete time step, radial modes computed using a spherical harmonic transform, and appearing in the exact nonreflecting boundary condition for the near-field solution, are imposed as Cauchy data for the radial wave equation in the exterior region outside the artificial boundary. The radial modes in the far-field are computed using an explicit finite difference solver and the method of characteristics. The exterior radial grid is truncated at the far-field point of interest with an exact NRBC expressed in modal form. This NRBC involves first-order derivatives only and does not require saving past values of the solution, which would be required in a Kirchoff-type time convolution. The solution at any point in the far-field is then computed from a spherical harmonic expansion of the far-field radial modes. In practice, the number of modes N included in this expansion is the same as the number of harmonics used in the NRBC. In computation, we have found $N \leqslant 25$ is usually sufficient for accurate solutions. If a large number of harmonics N are needed, the work required could be reduced by an order of magnitude using recently developed fast spherical transform algorithms. If the far-field point is sufficiently distant from the source of scattering, such that $kR_0 \gg n^2+1$, where $k = \omega/c$ is the nondimensional frequency and R_0 is the radius of the far-field point, then the exact boundary condition may be simplified a-priori to the asymptotic form of the NRBC, i.e., the local B_1 condition.

Far-field computations may be performed using two different approaches. One method is to first solve the near-field solution using the exact NRBC, then, based on the the solution for the modes $\phi_{nm}(R,t)$ on the artificial boundary, the exterior solution may be computed as a *post-process*. This two-stage approach enables great flexibility in the computation of far-field points of interest, however, for moderate to long time intervals, the amount of storage required for this two-stage process may become excessive. To address this problem, an efficient algorithm is given where the modes $\phi_{nm}(R,t)$ are computed as needed, and the far-field is solved *concurrently* with the near-field solution and the NRBC.

Numerical studies were performed and compared to analytical solutions to assess the accuracy of the method, both for individual harmonics, and for radiation and scattering problems involving an infinite number of harmonics. The results demonstrate that the concurrent method is highly accurate and efficient for direct time-domain computations of far-field solutions. The numerical results also confirm that the exact NRBC reduces to the local B_1 condition for far-field points sufficiently removed from the source of radiation/scattering. However, for a wide range of intermediate points, the use of exact nonreflecting boundary conditions for both near-field and far-field solutions shows significant improvement in accuracy over the local B_1 condition. Further computational efficiency may be obtained by replacing the exact NRBC with the asymptotic form given in (28), and recently descibed in [16]. In this form, the radial order may be lowered to reduce the number of auxiliary equations needed for high accuracy.

Acknowledgements

Support for this work was provided by the National Science Foundation under Grant CMS-9702082 in conjunction with a Presidential Early Career Award for Scientists and Engineers (PECASE), and is gratefully acknowledged. We would also like to thank the anonymous reviewer for helpful suggestions for improving the clarity of the manuscript.

References

[1] K.M. Mitzner, Numerical solution forvtransient scattering from a hard surface of arbitrary shape – retarded potential technique, J. Acoust. Soc. Am. 42 (1967) 391–397.
[2] C.L.S. Farn, H. Huan, Transient acoustic fields generated by a body of arbitrary shape, J. Acoust. Soc. Am. 43 (1968) 252–257.
[3] H. Huan, G.C. Everstine and Y.F. Wang, Retarded potential techniques for the analysis of submerged structures impinged by weak shock waves, in: T. Belytschko, T. Geers (Eds.), Computational Methods for Fluid-Structure Interaction Problems, ASME AMD 26, 1977.
[4] P.H.L. Groenenboom, Solution of the retarded potential equation and numerical stability, in: C.A. Brebbia (Ed.), Boundary Elements VI. in: Proceedings of the Sixth International Conference, July 1984.
[5] C.T. Dyka, R.P. Ingel, G.C. Kirby, Stabilizing the retarded potential method for transient fluid-structure interaction problems, Int. J. Numer. Methods Engrg. 40 (1997) 3767–3783.
[6] D. Givoli, Numerical methods for problems in infinite domains, Studies in Applied Mechanics, 33, Elsevier, Amsterdam, 1992.
[7] S. Tsynkov, Numerical solution of problems on unbounded domains: A review, Appl. Numer. Math. 27 (1998) 465–532.
[8] A. Bayliss, E. Turkel, Radiation boundary conditions for wave-like equations, Commun. Pure Appl. Math. 33 (1980) 707–725.
[9] P.M. Pinsky, N.N. Abboud, Finite element solution of the transient exterior structural acoustics problem based on the use of radially asymptotic boundary operators, Comput. Methods Appl. Mech. Engrg. 85 (1991) 311–348.
[10] P.M. Pinsky, L.L. Thompson, N.N. Abboud, Local high-order radiation boundary conditions for the two-dimensional time-dependent structural acoustics problem, J. Acoust. Soc. Am. 91 (3) (1992) 1320–1335.
[11] L.L. Thompson, P.M. Pinsky, A space-time finite element method for the exterior acoustics problem, J. Acoust. Soc. Am. 99 (6) (1996) 3297–3311.
[12] M.J. Grote, J.B. Keller, Exact nonreflecting boundary conditions for the time dependent wave equation, SIAM J. Appl. Math. 55 (1995) 280–297.
[13] M.J. Grote, J.B. Keller, Nonreflecting boundary conditions for time dependent scattering, J. Comput. Phys. 127 (1996) 52–65.
[14] L.L. Thompson, R. Huan, Implementation of exact nonreflecting boundary conditions in the finite element method for the time-dependent wave equation, Comput. Methods Appl. Mech. Engrg. 187 (2000) 137–159.
[15] L.L. Thompson, R. Huan, Finite element formulation of exact nonreflecting boundary conditions for the time-dependent wave equation, Int. J. Numer. Methods Engrg. 45 (1999) 1607–1630.
[16] R. Huan, L.L.Thompson, Accurate radiation boundary conditions for the time-dependent wave equation on unbounded domains, Int. J. Numer. Methods Engrg. 47 (2000) 1569–1603.
[17] T. Hagstrom, S. Hariharan, A formulation of asymptotic and exact boundary conditions using local operators, Appl. Numer. Math. 27 (1998) 403–416.
[18] B. Alpert, L. Greengard and T. Hagstrom, Rapid evaluation of nonreflecting boundary kernels for time-domain wave propagation, SIAM J. Numer. Anal., in press.
[19] J.P. Berenger, A perfectly matched layer for the absorption of electromagnetic waves, J. Comput. Phys. 114 185–200.
[20] X. Yuan, D. Borup, J.W. Wiskin, M. Berggren, R. Eidens, S.A. Johnson, Formulation and validation of berengers PML absorbing boundary for the FDTD simulation of acoustic scattering, IEEE Trans. Ultrason. Ferro Freq. Control. 44 (4) (1997) 517–522.
[21] L. Ting, M. Miksis, Exact boundary conditions for scattering problems, J. Acoust. Soc. Am. 80 (1986) 1825–1827.

[22] D. Givoli, D. Kohen, Nonreflecting boundary conditions based on Kirchoff-type formulae, J. Comput. Phys. 117 (1995) 102–113.
[23] J.B. Keller, D. Givoli, Exact nonreflecting boundary conditions, J. Comput. Phys. 82 (1989) 172–192.
[24] L.W. Pearson, R.A. Whitaker, L.J. Bahrmasel, An exact radiation boundary condition for the finite-element solution of electromagnetic scattering on an open domain, IEEE Trans. Magn. 25 (4) (1989) 3046–3048.
[25] I. Sofronov, Conditions for complete transparency on the sphere for the three-dimensional wave equation, Russian Acad. Sci. Dokl. Math. 46 (1993) 397–401.
[26] I. Sofronov, Artificial boundary conditions for absolute transparency for two- and three-dimensional external time-dependent scattering problems, Euro. J. Appl. Math., 1999.
[27] L. L. Thompson, P. M. Pinsky, New space-time finite element methods for fluid-structure interaction in exterior domains, Comput. Methods Fluid/Structure Interac. AMD-vol. 178, ASME (1993) 101–120.
[28] L.L. Thompson, P.M. Pinsky, A space-time finite element method for structural acoustics in infinite domains, part 2: Exact time-dependent non-reflecting boundary conditions, Comput. Methods Appl. Mech. Engrg. 132 (1996) 229–258.
[29] H. Lamb, Hydrodynamics, fourth Ed., Cambridge University Press, Cambridge, 1916, p. 517, Eq. (4).
[30] L.L.Thompson and R.Huan, Accurate radiation boundary conditions for the two-dimensional wave equation on unbounded domains, submitted 1999.
[31] N.N. Abboud, G.L. Wojcik, D.K. Vaughan, J. Mould, D.J. Powell, L. Nikodym, Finite Element Modeling for Ultrasonic Transducers, Proc. SPIE Int. Symp. Medical Imaging 1998, Ultrasonic Transducer Engineering Conference, San Diego, CA., 21–27 Feb., 1998.
[32] A.S. Lyrintzis, Review: the use of Kirchoffs method in computational aeroacoustics, J. Fluids Engrg. 116 (12) (1994) 665–676.
[33] J.P. Wright, Direct time integration methods for structural acoustics and far-field scattering computations, ASME J. Vib. Acoust. 117 (1995) 488–492.
[34] A. Sommerfeld, Partial Differential Equations in Physics, Academic Press, New York, 1964.
[35] M.J. Mohlenkamp, A fast transform for spherical harmonics, Preprint, 1997.
[36] J. Driscoll, D. Healy, D. Rockmore, Fast discrete polynomial transforms with applications to data analysis for distance transitive graphs, SIAM J. Comput. 26 (1997) 1066–1099.
[37] M. Abramowitz, I. Stegun, (Eds.), Handbook of Mathematical Functions, Washington, DC: National Bureau of Standards, 1964. Reprinted by Dover Publications, New York, 1968, pp. 751–770.
[38] W. Strauss, L. Vazquez, Numerical solution of a nonlinear Klein–Gordon equation, J. Comput. Phys. 28 (1978) 271–278.
[39] P.M. Morse and H. Feshbach, Methods of Theoretical Physics, vol. II, McGraw-Hill, New York, 1953.
[40] N.H. Ricker, Transient Waves in Visco-Elastic Media, Elsevier, Amsterdam, Netherlands, 1977.
[41] P.R. Stepanishen, Transient radiation from pistons in an infinite planar baffle, J. Acoust. Soc. Am. 49 (1971) 1629–1638.